DEFINITIONS OF CLEAR-SKY FLUXES AND IMPLICATIONS

A Thesis

by

ABHISHEK VERMA

Submitted to the Office of Graduate Studies of
Texas A&M University
in partial fulfillment of the requirements for the degree of

MASTER OF SCIENCE

December 2011

Major Subject: Atmospheric Sciences

DEFINITIONS OF CLEAR-SKY FLUXES AND IMPLICATIONS

A Thesis

by

ABHISHEK VERMA

Submitted to the Office of Graduate Studies of
Texas A&M University
in partial fulfillment of the requirements for the degree of

MASTER OF SCIENCE

Approved by:

Chair of Committee,	Andrew Dessler
Committee Members,	Ping Yang
	Gerald R. North
	Ping Chang
Head of Department,	Kenneth Bowman

December 2011

Major Subject: Atmospheric Sciences

ABSTRACT

Definitions of Clear-sky Fluxes and Implications. (December 2011)
Abhishek Verma, B. Tech, Indian Institute of Technology Madras; M. Tech, Indian Institute of Technology Madras
Chair of Advisory Committee: Dr. Andrew Dessler

Clear-sky top-of-atmosphere (TOA) fluxes are important in estimating the impact of clouds on our climate. In this study, we quantitatively compare the clear-sky fluxes measurements of the Clouds and the Earths Radiant Energy System (CERES) instrument to clear-sky fluxes from two reanalysis, NASA's Modern Era Retrospective-analysis for Research and Application (MERRA), and the European Center for Medium Range Weather Forecast Interim reanalysis (ERA-Interim). In the first comparison, we compare observed fluxes from individual cloud-free field-of-views to the reanalyses. In the second comparison, we compare monthly averaged observed clear-sky fluxes to those from the reanalyses. Monthly clear-sky fluxes are calculated by averaging fluxes from cloud-free regions.

In both comparisons, the fluxes generally agree within $\pm$ 10 W/m^2. Finally, we show that, while the differences between the fluxes of observations and the reanalyses are several W/m^2, the inter-annual anomalies agree much better, with zonal and global average inter-annual anomalies typically agreeing within 1 W/m^2. The longwave clear-sky anomalies show excellent agreement even when comparing individual grid points, whereas the shortwave clear-sky anomalies are generally smaller at individual grid points.

ACKNOWLEDGMENTS

I would like to express my heartfelt gratitude to lots of people without whom I would not have succeeded in this program. First of all, I would like to thank my guide, Prof. Andrew E. Dessler, for his guidance and support throughout the course of my program. He has given me valuable insights in doing research, and for this I am indebted to him. I also thank him for his encouragement and support during hard times, and appreciate his valuable suggestions to help me progress in my research.

I express my sincere appreciation for the faculty and the staff members of the Department of Atmospheric Sciences. Their intuitive teaching, supervision and guidance have been helpful throughout the course of my study. I thank my fellow graduate students for always keeping up the spirit of research with their lively and entertaining discussions.

I am indebted to all my friends at the Texas A&M University for making my stay an experience worth cherishing. Finally, I am thankful for my parents, my sister and my fiancee for their unconditional love and motivation that will always shelter me in tough times.

NOMENCLATURE

ADM	Empirical Angular Distribution Model
CERES	Clouds and Earth Radiant Energy System
CRF	Cloud Radiative Forcing
EBAF	Energy Balanced And Filled
ECMWF	European Center for Medium-range Weather Forecast
EOF	Empirical Orthogonal Function
ERA	ECMWF Re-Analysis Project
ERA-40	ECMWF 40-year Reanalysis
ERBE	Earth Radiation Budget Experiment
FOV	Field-of-View
GCM	Global Circulation Model
GHG	Greenhouse Gase
ITCZ	Inter Tropical Convergence Zone
LW	Longwave
MERRA	Modern Era Retrospective-analysis for Research and Application
MODIS	Moderate Resolution Spectroradiometer
NASA	National Aeronautics and Space Administration
NMC	National Meteorological Center
OLR	Outgoing Longwave Radiations
RSW	Reflected Solar Radiations
SSF	Single Scanner Footprint
SW	Shortwave
TOA	Top-of-atmosphere
WN	Window

TABLE OF CONTENTS

Page

Page

LIST OF TABLES

LIST OF FIGURES

FIGURE Page

FIGURE Page

1. INTRODUCTION

Understanding the global climate system has gained immense momentum in recent decades. Climatological assessments prove to be important in studying anthropogenic impacts, forecasting earth's climate, evaluating regional implications of climate related phenomena etc. Typically, current scenarios of global warming, mountain glacier depletion, occurrence of hazardous weather pattern, to name a few, are issues on which significant resources and infrastructure have been implemented to understand, assess and apply mitigation methods. One of the important means of analysis in climate sciences is working with the radiation budget of the earth.

The radiation budget represents energy transactions that play an important role in defining the earth's climate state. It explains the energy exchange that our planet experiences with its surrounding (the Sun and the outerspace). This includes balance of radiational energy from the sun categorized as shorter wavelength radiation (or shortwave radiation) and thermal radiations emitted by the earth system, identified as radiation of longer wavelength (or longwave radiation). It also explains the energy flow within the earth-atmosphere system; attenuation of incoming solar radiation by clouds, aerosol content, land surfaces, snow and ice caps etc. absorption of thermal radiations by clouds, greenhouse gases etc. Pertinent components of radiation budget are quantified using observational suites and model ensembles. Data from observation systems such as satellite system, radiosonde, solar panels etc. and simulation results from model generated scenarios including climate-model, reanalysis with assimilation system, radiative transfer models, to name a few, have helped in establishing our scientific perceptions in these areas.

This thesis follows the style of *the Journal of Geophysical Research*.

The energy transfers are commonly interpreted in terms of radiative fluxes. Radiative fluxes map the energy transmitted in radiances at various wavelengths towards or away from the earth system. Various studies have estimated the distribution of these fluxes at top-of-atmosphere (TOA), over land, ocean and ice-covered surfaces, in both upwelling and downwelling direction. Various agents present in the atmosphere such as aerosols, clouds, greenhouse gases (GHG) interact with these fluxes and alter their distribution causing radiative forcings. By convention, a positive forcing represents a net incoming energy flux whereas a negative forcing represents a net energy loss. These forcings can create significant perturbation in the atmospheric state as well as in the climate. This make agent properties pertinent in establishing a thorough knowledge of sciences involved in the climate system. One such agent which is highly sought after is the clouds.

1.1 Cloud Radiative Forcing

Clouds play an important role in defining our climate as they participate in the radiational balance. They reflect the incoming shortwave radiations, cooling the earth's surface and absorb the emitted thermal longwave radiation, warming the atmosphere underneath. A common metric for quantifying the radiative impact of clouds is cloud radiative forcing or CRF, which is conventionally defined as:

$$CRF = R_{clear-sky} - R_{all-sky}$$

where $R_{all-sky}$ is the TOA net flux and $R_{clear-sky}$ is the TOA net flux when clouds do not participate. CRF, in general, represents a first order estimate of cloud influence on radiational distribution of the planet. It is correlated with cloud properties such as cloud distribution, cloud height, cloud fraction, cloud thickness etc. For example, clouds present at lower heights produce a net cooling effect underneath by reflecting incoming solar radiation. They have almost the same temperature as the land

surface underneath which create a negative radiative forcing. On the other hand, cirrus clouds present at high altitude produce a positive radiative forcing by absorbing longwave radiation emitted from the earth's surface. Hence, changes in cloud properties are reflected in changes in CRFs which makes it pertinent in studying climate variations.

Analyzing CRF serves the purpose of quantifying the effect of clouds on the climate state. Since, the cloud system is intricately woven with the earth's climate, cloud responses are often studied as feedbacks. However, quantifying cloud feedbacks is very challenging as cloud radiative interactions poses large uncertainties. Work done by *Soden and Held* [2006] suggests disagreements in cloud-feedback values predicted by various twenty-first-century climate models. Short term cloud feedback inferred in the recent work of *Dessler* [2010], which uses satellite observations and reanalysis data, also incorporates significant uncertainty to the predicted value. These uncertainties are very likely associated with uncertainties in CRFs, as net TOA flux anomalies due to cloud feedback are well correlated with CRFs anomalies [see *Dessler*, 2010, Fig. 1b]. Therefore, we base our study on analyzing the quality of clear-sky fluxes available from various sources, which are pertinent in estimating CRFs.

1.2 Clear-sky Fluxes

We define clear-sky fluxes as radiative fluxes that exclude participation of clouds in the radiation budget. These fluxes (shortwave and longwave) are constructed using radiances that aren't attenuated by cloud hydrometeors and are used in determining CRFs. By far, clear-sky fluxes are derived using two approaches based on (i) satellite measurements and (ii) model generated data. Satellite-based fluxes treat clear-sky conditions strictly based on the observational record. This approach classifies TOA fluxes observed over cloud-free satellite footprints as clear-sky fluxes. CRF is then defined as difference in TOA flux for all observations from cloud-free measurements.

It is important to mention here, that instruments record radiance emerging from a specific area on the earth's surface at a given point of time. This limits the satellite from reporting TOA fluxes emerging all over the globe at a given instant. However, global climatologies of fluxes are created using observations recorded in a given time frame. Such distribution are considered time-averaged quantities.

Model based clear-sky fluxes, on the other hand, are estimated using radiative transfer calculations with zero cloud optical depth. They take into account factors such as surface temperature, albedo, aerosol content, GHG concentrations, temperature and humidity profile, dynamical structure etc. in their calculation. These simulations, without altering the atmospheric concentrations, omit any physical participation of clouds in attenuating radiations. The advantage in this approach is that a complete global climatology is available at each model time step.

In the following sections, we intend to clarify issues regarding clear-sky fluxes. Our study compares upwelling TOA clear-sky fluxes derived from satellite measurements and model simulation. Section 2 describes the satellite-derived clear-sky fluxes which we use in our analysis followed by Section 3 on model-derived clear-sky fluxes. Section 4 draws the difference in the global distribution of fluxes followed by Section 5 which looks into inter-annual variability in clear-sky fluxes.

2. SATELLITE-INFERRED CLEAR-SKY FLUXES

Radiometer onboard a satellite measures radiances emerging at the top of the earth's atmosphere from various wavelengths. For the purpose of flux measurements, broadband instruments are used to record radiances across a wide spectral range. Radiative fluxes corresponding to shortwave, longwave and infrared window channels are measured frequently from such platforms. One such operational instrument which we use is the CERES instrument onboard NASA's Terra satellite. This section briefly explains the CERES instrument and its data product from which clear-sky data were extracted. Typical global flux distribution from such data products will also be shown here.

2.1 CERES Instrument

This instrument is a broadband radiometer that uses precision thermistor bolometers for radiance measurement [*Wielicki et al.*, 1996]. It comprises three channels to record filtered radiance. They are (i) the 0.2μm to 5μm channel which measures radiances categorized as SW, (ii) the total channel measuring radiance from 0.2μm to 200μm and (iii) the infrared window channel that observes from 8μm to 12μm wavelength. These radiances are converted for imperfect spectral response of CERES to unfiltered radiances of reflected SW, emitted terrestrial LW and window radiations. In particular, LW radiances are inferred using total channel reading depending on daytime or nighttime observation. Daytime LW radiance are calculated by subtracting total channel radiance from SW channel radiance where as nighttime observation involve only the total channel reading as SW radiance are absent.

Computing TOA fluxes requires the accounting for anisotropy of instantaneous CERES radiances. This angular dependence makes the radiance field a strong function of optical and physical characteristics of the viewed scene (e.g. surface albedo, cloud phase, aerosol optical depth, etc.) Hence, ADMs are constructed using scene-

type parameters of MODIS measurements to facilitate radiance-to-flux conversion. *Loeb et al.* [2005] and *Loeb et al.* [2007] provide us with the methodology and validation procedure used in constructing the ADMs for CERES instrument onboard Terra satellite.

Many CERES datasets constructed from onboard measurements are available, based on the level of data processing involved. For the purpose of our study, CERES-SSF and CERES-EBAF datasets were used and the following subsections describe them in detail.

2.1.1 CERES-SSF

CERES-SSF is a Level-2 dataset constructed from CERES instrument observations [*Smith et al.*, 2011]. This product combines CERES measurements with scene information from high resolution imager such as VIRS for TRMM satellite or MODIS for Terra and Aqua satellite. The imager pixel data are convolved into CERES footprint giving quantitative estimates of cloud-related parameters. This is unlike ERBE dataset where each scene is qualitatively categories as clear, partly cloudy, mostly cloudy or overcast. SSF dataset provides information on FOV geometry and viewing angles, channel radiances, TOA radiative fluxes, clear and cloudy area statistics, imager radiance statistics and MODIS aerosol parameters.

In our analysis, CERES-SSF cloud-free measurements were used in constructing global distributions. Cloud-free footprints were sorted from the dataset using the 'Cloud mask clear-strong percent coverage' parameter as mentioned in *Dessler et al.* [2008]. This parameter was set to a threshhold of 96% and above for cloud-free classification within SSF datasets. Also, the 'Radiance and Mode flags' of each footprint was checked to ensure good quality radiances. Meeting this criteria, all the footprints were selected, arranged and averaged on 1^o by 1^o lat-lon grid over the globe. The uncertainty of an individual top-of-atmosphere measurement was found

to be 10 W/m^2 in SW and 3-5 W/m^2 in LW by *Loeb et al.* [2007], where as regional average of measurements have relatively lower uncertainty.

2.1.2 CERES-EBAF

A Level-4 product, CERES-EBAF provides monthly average flux distributions. This dataset has adjusted flux data to reflect the best estimate of net radiational imbalance at TOA from *Hansen et al.* [2005]. An objective constrainment algorithm is employed to adjust both LW and SW TOA fluxes, each within their range of uncertainty, to match the global net imbalance. *Loeb et al.* [2009] gives a detailed description on the construction of CERES-EBAF fluxes based on the error analysis of TOA fluxes from CERES monthly mean data products.

For the purpose of our analysis, we choose the monthly averaged flux distribution for the period of March 2000 to October 2005. An EBAF clear-sky TOA climatology reflects cloud-free regions at both CERES footprint and sub-CERES footprint scale. This is done by converting the MODIS cloud-free radiances available over partly or mostly cloudy CERES footprint to broadband radiance. These 'broadband' MODIS radiances are then converted to TOA radiative fluxes using CERES clear-sky ADMs [*Loeb et al.*, 2005] and included in the compilation. Such distribution, as will be discussed later, results in a reduction of dry biases generally observed in satellite-derived clear-sky fluxes and can be useful in evaluation of climate-model outputs. Also, this method helps in improving the clear-sky flux coverage unlike other monthly flux data products.

2.2 Clear-sky Flux Distribution

This subsection describes the clear-sky flux distribution constructed from CERES measurements. Our data correspond to Flight Model 1 measurements made onboard NASA's Terra satellite. Figure 2.1 and 2.2 show the regional distribution of monthly

mean clear-sky fluxes from SSF and EBAF datasets. Figure 2.1 correspond to upwelling TOA LW fluxes originating from cloud-free scenes for the month of January and July, 2008. Top panels depict SSF distributions with EBAF in the bottom panels.

Region of high $\mathrm{OLR}_{clear-sky}$ (above 300 W/m^2) are commonly seen in the tropics. In January, Australia, the Indian Peninsula, eastern and southern Africa and southern South America show high $\mathrm{OLR}_{clear-sky}$ regions over land. Regions of lower $\mathrm{OLR}_{clear-sky}$ concentration (below 240 W/m^2) are indicated above 30^o N. Whereas, in the southern hemisphere, such regions occur beyond 60^o S, towards the south pole due to low surface temperatures. Over oceans, high $\mathrm{OLR}_{clear-sky}$ regions in the tropics occur in coherence with subsidence regions of the Hadley circulation.

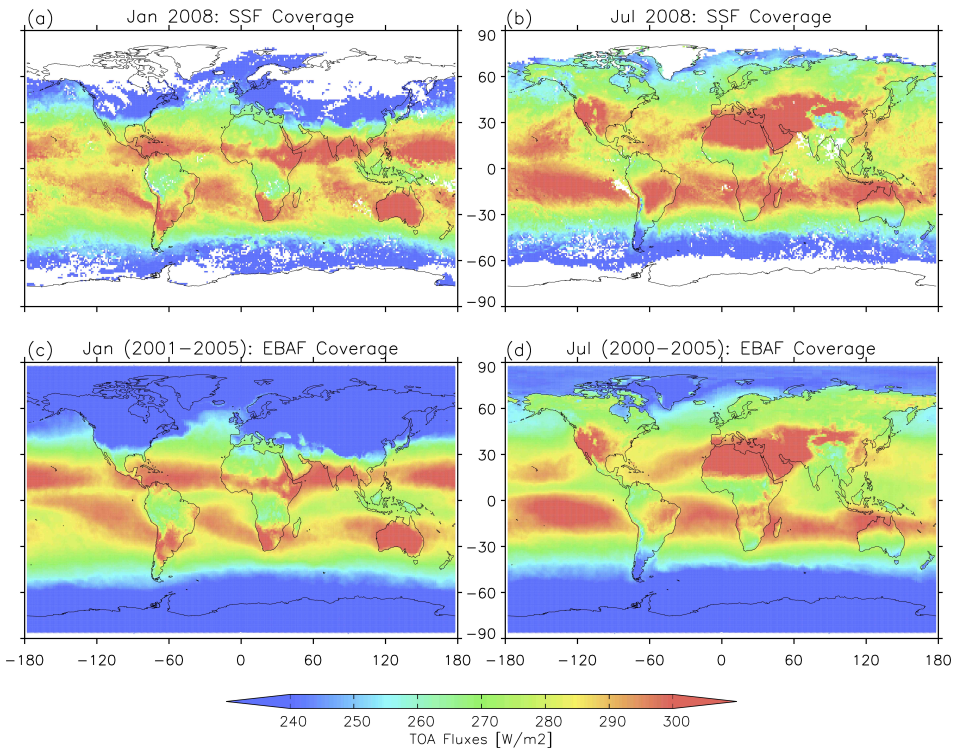

Fig. 2.1. Typical $\mathrm{OLR}_{clear-sky}$ distribution in January and July of (a),(b) CERES-SSF and (c),(d) CERES-EBAF product.

In July, high $\text{OLR}_{clear-sky}$ regions occur over western Asia, the Saudi Arabian Peninsula, the Saharan Desert over northern Africa, parts of southern Africa, western North America and eastern South America continent. Particularly over the oceans, the Hadley subsidence regions in the southern hemisphere show high $\text{OLR}_{clear-sky}$ signatures (0^o to 30^oS latitude zone) in addition, to regions over the northern Pacific and Atlantic Ocean. Low $\text{OLR}_{clear-sky}$ magnitude are observed mostly over the southern hemisphere with the Greenland in the north.

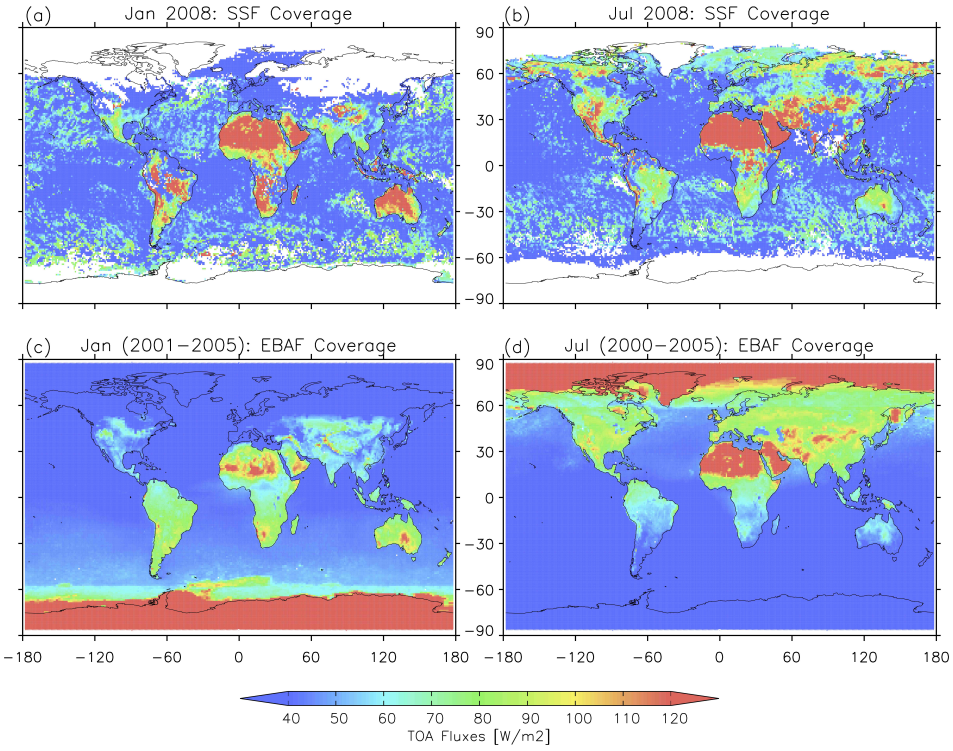

Fig. 2.2. Typical $\text{RSW}_{clear-sky}$ distribution in January and July of (a),(b) CERES-SSF and (c),(d) CERES-EBAF product.

Figure 2.2 depicts the distribution of TOA SW fluxes from the datasets. SSF depiction of clear-sky SW fluxes are shown to be different from EBAF. Regions of high SW fluxes are exaggerated by SSF over land coupled with noisy distribution over

the oceans. In January, Australia, Africa and South America show higher SW fluxes (above 100 W/m^2) as compared to EBAF datasets. With solar insolation playing an important role, the Antarctica is shown to have high flux concentration by reflection from snow/ice surfaces. Oceans show low SW concentration over most parts of the globe with exception to sea-ice region near the Antarctica. In all, a contrast in the surface albedo properties of land and ocean emerges which is also noticeable in July.

For the month of July, the northern hemisphere shows high SW fluxes as compared to the southern hemispheric continents. The Saharan Desert and the regions near the north pole depict high SW reflection. Patches of high SW fluxes also appear over high elevation regions such as the Tibetan Plateau and the Rockies in North America.

Note that the SSF sampling have missing regions towards the pole and over areas with persistent cloudiness. Such pixels are avoided based on the selection criteria set for SSF clear-sky fluxes. On the other hand, EBAF has a complete global coverage as a result of filled values. Figure 2.1 and 2.2 are example of clear-sky flux distribution derived using satellite measurements. Different datasets have different representation of fluxes and it is important to consider the methodology used in constructing clear-sky fluxes. However, they reflect similarities in seasonal variation of flux distribution for many regions.

2.3 All-sky Flux Distribution

This subsection illustrates all-sky fluxes distribution derived from satellite measurements. All-sky fluxes here implies TOA fluxes measured in all possible cloud condition i.e. clear-sky, partly cloudy, mostly cloud and overcast scenes. Differences in all-sky and clear-sky flux distribution mainly arise as a result of cloud presence and we will highlight certain aspects of this quantity on regional scale. Figure 2.3 and 2.4 illustrate the regional all-sky flux distribution for LW and SW respectively,

using the same color scheme as that for clear-sky fluxes. Note that SSF all-sky fluxes shown here have complete coverage, unlike clear-sky fluxes.

From Figure 2.3, regions of high OLR are shown over central Australia, the Indian peninsula and Somalia, for January. High OLR regions over ocean are found mostly in the tropics, over the Pacific and the Arabian Sea. OLR distribution for July depicts a different picture, with high OLR regions shown over northern Australia, western Asia, northern Africa (the Saharan Desert), parts of western North America and eastern South America. The low OLR regions in the tropics mostly correspond to cloudy regions over south-eastern Asia, central Africa and central America. Due to greenhouse effect, high-altitude clouds reduce OLR emissions from the surface underneath and lowers the TOA flux values.

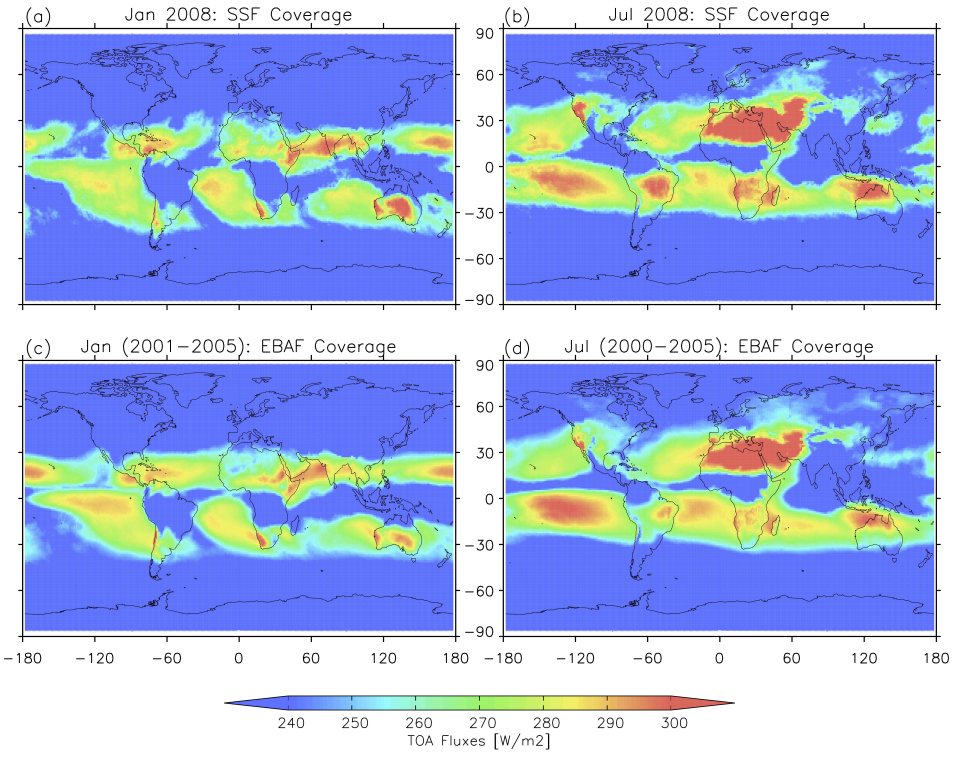

Fig. 2.3. Typical OLR_{allsky} distribution in January and July of (a),(b) CERES-SSF and (c),(d) CERES-EBAF product.

Figure 2.4 depicts TOA SW radiation for all observation, using the same color scheme as for clear-sky fluxes. Note the SW fluxes over polar regions which remain dark throughout the month in SSF dataset. These areas are beyond 60^o North for January and 60^o South for July. Likewise, these areas are filled in EBAF dataset with zero value. Clearly, a polarized distribution of RSW is seen as a result of solar insolation. High RSW regions are limited to the sunlit polar and continental regions for both months. Oceans in the tropics show high RSW owing to cloud top reflection, mostly along the convergence belt.

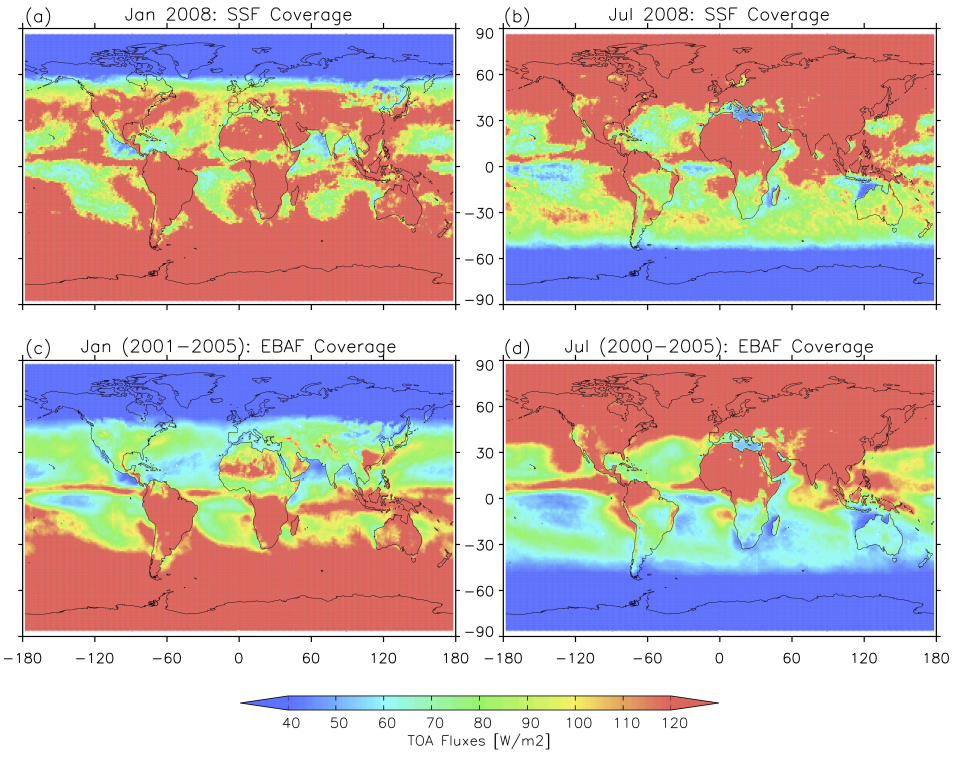

Fig. 2.4. Typical RSW_{allsky} distribution in January and July of (a),(b) CERES-SSF and (c),(d) CERES-EBAF product.

In January, Australia, southern Africa, South America and southeastern China are high in RSW concentration. The SSF distribution, though, have high RSW

values over most land regions and major parts of the ocean. This could be due to the lack of diurnal averaging in fluxes. Regions over the ocean, west of North America continent and the Indian Peninsular region show low RSW concentration. In July, most of the high RSW values are limited to the northern hemisphere and over land surfaces.

To summarize, we show an example of all-sky flux distributions constructed from CERES measurements. LW and SW upwelling fluxes were presented for the month of January and July. The fluxes illustrated here have dissimilarities owing to cloud presence which alters TOA radiations. Reduction in TOA flux magnitude and changes in regional distribution with respect to clear-sky fluxes are seen here. We will use the clear-sky flux distributions from these data products and compare them with reanalysis fluxes explained in the following section.

3. MODEL-DERIVED CLEAR-SKY FLUXES

Models calculate radiative fluxes using radiation scheme on atmospheric columns. They simulate fluxes at various level of the atmosphere, including surface, tropopause and TOA level. These fluxes correspond to all scenarios of cloud covering i.e. clear, broken and overcast, and differs from satellite-inferred clear-sky fluxes which include only cloud-free pixels. Yet, evaluating clear-sky TOA fluxes from GCMs with satellite observations is important for determining model performance and accuracy. This creates the need to apply different methods of sampling clear-sky fluxes which are consistent with satellite data processing.

3.1 Literature Review

Previous work by *Cess and Potter* [1986] had recognized two definitions of clear-sky fluxes possible from GCM models. These were Method 1 and Method 2 classification of clear-sky fluxes. As the authors suggest, Method 1 includes only clear-sky grid points in the model, thereby taking only cloud-free fluxes. Monthly mean of fluxes are determined by using this clear subset. Method 1 by virtue of its selection, does not include diurnal averaging of fluxes. Method 2, on the other hand, includes combination of fluxes calculated for cloud-free and overcast grid points, taking clear-sky calculations for overcast grid. This method incorporates diurnal averaging in estimating monthly mean fluxes and differs in tropospheric water vapor composition. This article also pointed out the importance of resolving diurnal cycle and fractional cloudiness at individual grid point for inferring accurate flux simulation which are comparable with satellite observations.

In regard with the previous definitions, *Cess et al.* [1992] explains the shortcoming of both the methods compared to the ERBE derived clear-sky fluxes. ERBE clear-sky fluxes pertain to observations from cloud-free footprint, which are processed through diurnal model. In comparison, Method 1 samples clear-sky grids without diurnal av-

eraging, where as Method 2 incorporates diurnal averaging with all grids, biasing the distribution towards moist conditions (as cloudy regions contain more tropospheric water vapor than clear-sky areas). *Cess et al.* [1992] proposes a Method 3 definition, which avoids grids of persistent cloudiness from Method 2. This definition selects only those grids which have clouds absent for one or more times in a given day, and assigns diurnally averaged Method 2 clear-sky flux for that day. This makes Method 3 more consistent with respect to ERBE clear-sky fluxes. Although, spatial and temporal resolution differences between model and satellite data can cause discrepancies in flux distribution. Proceeding further, *Zhang et al.* [1994] proposes a Method 4 definition, which takes into account the correlation of cloudiness and clear-sky pixel fraction in a model grid.

Due to differences in approach, satellite and model-derived clear-sky fluxes must be made consistent with one another. In our study, we address this issue taking consistent datasets for comparisons. CERES-EBAF dataset contains information from both clear and cloudy footprints, similar to model diagnostics used. In place of model-derived fluxes, we use fluxes from the latest generation of reanalysis. Clear-sky fluxes from reanalysis data incorporate observational based information on the atmospheric state. Reanalysis is know to produce realistic large scale circulations which are spatially consistent with radiation budget data, unlike most of the climate models. The following subsection describes a generic reanalysis system and the types used in our study.

3.2 Reanalysis System

Reanalysis data are those produced by assimilating observational data in initializing numeric weather forecasts. An important feature of reanalysis data is that it is produced using fixed version of a data assimilation system along with the forecast model, unlike the archived weather analyses from operational systems. The main importance of a reanalysis is that it provides a coherent and spatially complete record

of the global atmospheric structure. The dynamical fields estimated by reanalysis are more likely consistent with the law of physics as well as with the observations (within their uncertainties). These data are, thereby, used in the context of meteorology-related studies and have proved to be of great value. In addition, reanalysis records have effective been used in climate-related research and are been frequently used in studying atmospheric trends in climate time series.

The ability to produce a homogenous record of atmospheric variability provides the opportunity to estimate climate trends on inter-annual and decadal time scales. By operating with a fixed assimilation system, reanalysis avoids discrepancies in long-term data due to shifts and spurious signals introduced in operational analyses by system upgrades. Yet, changes in assimilated observing system and time varying biases in model and observations, affect the quality of long-term data. Therefore, it is important to identify and interpret the climate-quality of reanalysis. Our study provides a quantitative assessment of the performance of reanalysis, against observation-only climate datasets. For this purpose, we use the latest available reanalysis product.

3.2.1 MERRA Reanalysis

MERRA is NASA's atmospheric reanalysis which uses the latest version of the Goddard Earth Observing System Data Assimilation System, version 5 [*Rienecker et al.*, 2008]. It is aimed at producing historical analyses of the hydrological cycle in weather and climate scales assimilating NASA's satellite radiances. MERRA specifically covers the satellite era starting from 1979 and extending the analysis as more satellite observation becomes available in future. The analysis is available at a horizontal resolution of $2/3^o$ longitude by $1/2^o$ latitude supported by 72 vertical levels, extending upto 0.01 hPa. In addition, hourly two-dimensional diagnostic fields are also available, such as TOA fluxes, at native horizontal resolution. Hourly TOA fluxes derived can, therefore, be compared with instantaneous satellite observations.

Monthly mean for diagnostic fields are also available, along with global, zonal and regional distribution. Most of the MERRA data used here were retrieved online through the Goddard Earth Sciences Data and Information Services Center.

The radiative transfer model used in GEOS-5 is that of the prototype version of the Community Radiative Transfer Model (except for the historical Stratospheric Sounding Unit data stream). This model is used to address four main component involved in radiative transfer, which are (i) atmospheric gaseous absorption, (ii) scattering and absorption by clouds and aerosols, (iii) surface optics - emissivity and reflectivity and (iv) the radiative transfer solution. In particular, the cloud and precipitation optical parameters are evaluated with the general Mie Theory using modified gamma distribution function. The radiative transfer models deals with hydrometers including cloud ice, cloud liquid water, snow, graupel, hail and rain water in simulating radiances. Finally, the solver module solves the radiative transfer equation for determined atmospheric optical depth profile, surface emissivity and reflectivity, cloud optical parameters and source function.

3.2.2 ERA-Interim

ERA-Interim is the latest atmospheric reanalysis of ECMWF covering the period from 1 January 1988 and extending in near-real time analysis [*Dee et al.*, 2011]. Using 12-hourly analysis cycle, it combines observations with prior information from forecast model. Following this, a variational analysis is performed to estimate the evolving state of the atmosphere and a short-range model forecast is projected, providing the prior state for next analysis cycle.

ERA-Interim employs a 4D variational analysis scheme, unlike ERA-40, which results in more effective usage of observations from data assimilation. A variational bias correction scheme is also included in correcting biases from satellite radiance and minimizing inconsistencies among various observations. ERA-Interim forecast model is based on the released version Cy31r2. The atmospheric model used here is

of spectral T255 horizontal resolution with 60 vertical model layers extending upto 0.1hpa, operating in 30 minute time steps. The ERA-Interim archive contains 6-hourly gridded, three-dimensional meteorological variable with 3-hourly estimates of two-dimensional field. The TOA flux analyses were available at a horizontal resolution of 1.5^o by 1.5^o averaged over a 3 hourly period. Radiative transfer modeling and further details on ERA-Interim is present in *Dee et al.* [2011]. Prognostic information from forecast model were used in the radiation scheme, whereas climatological information of aerosol, trace gases, carbon dioxide and ozone were employed.

3.3 Clear-sky from Reanalysis

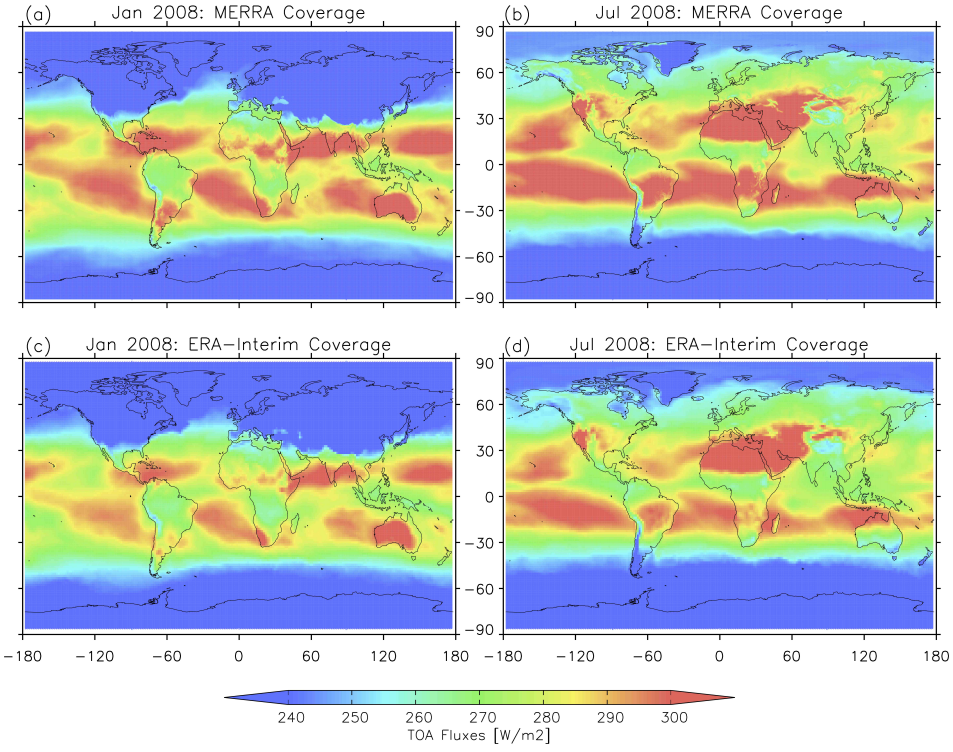

Fig. 3.1. Typical $OLR_{clear-sky}$ distribution in January and July of (a),(b) MERRA and (c),(d) ERA-Interim product.

This subsection gives an illustration of the regional clear-sky fluxes simulated by MERRA and ERA-Interim reanalysis. The intention here is to present qualitative similarities in clear-sky fluxes derived from two distinct source (satellite measurements and model). Figure 3.1 and 3.2 show the upwelling TOA clear-sky fluxes in LW and SW spectrum respectively. $\mathrm{OLR}_{clear-sky}$ distribution shown in Figure 3.1 is similar in many aspects to satellite-derived fluxes (here CERES-EBAF) in the month of January and July, 2008. High $\mathrm{OLR}_{clear-sky}$ regions are visible in the tropics, prominently over subsidence areas. Patterns of OLR concentration over land domain are also found to be similar in the reanalyses. While, MERRA and ERA-Interim exhibit some differences over ocean regions where high $\mathrm{OLR}_{clear-sky}$ are found.

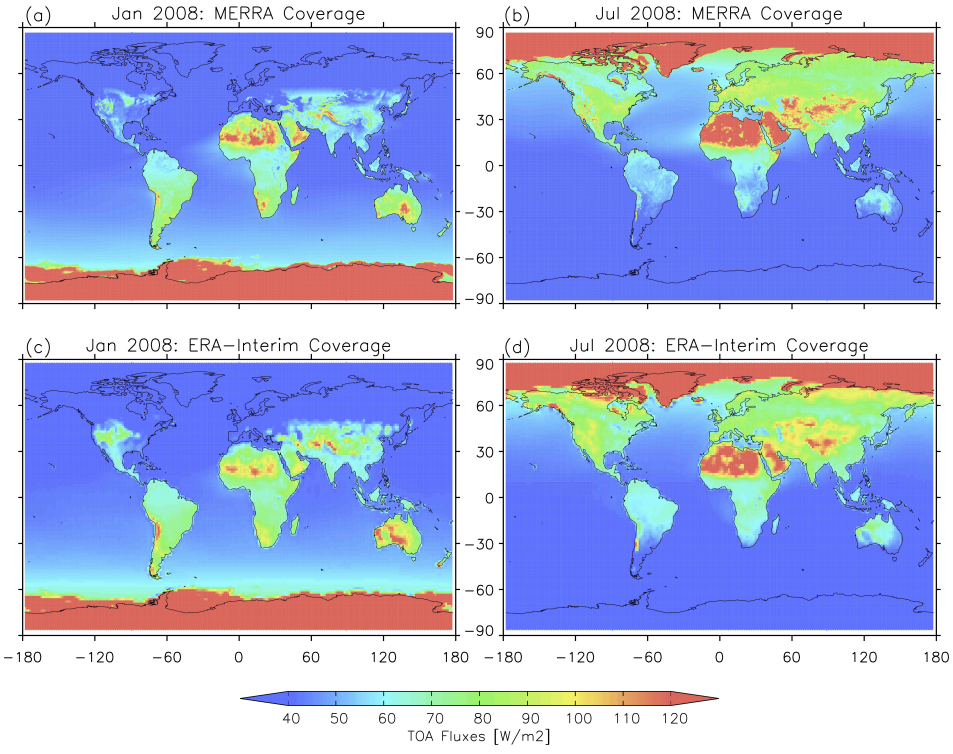

Fig. 3.2. Typical $\mathrm{RSW}_{clear-sky}$ distribution in January and July of (a),(b) MERRA and (c),(d) ERA-Interim product.

Figure 3.2 shows the $\mathrm{RSW}_{clear-sky}$ distribution in MERRA and ERA-Interim reanalysis. Similar to Figure 2.2, the contrast in land and ocean surfaces is highlighted here. Seasonal variation among the two month is depicted with summer time polar regions having high levels of $\mathrm{RSW}_{clear-sky}$. Desert region of the Sahara, the Saudi Arabian Peninsula and parts of central Asia are marked in both months, depicting high surface albedo values in the model.

In our study, we use MERRA and ERA-Interim reanalysis and compare them with observational fluxes. The modelling aspect of the two are quite distinct from one another. Nevertheless, these are the latest reanalysis available in the field of atmospheric sciences having improved model schemes in global hydrological cycle, atmospheric, land surface and ocean model, forecast-assimilation system etc. It is assured that these are markedly better than their previous version for most part.

4. COMPARISONS OF CLEAR-SKY FLUXES

This section describes our analysis on contrasting flux distribution from reanalysis data with satellite measurements. Both MERRA and ERA-Interim fluxes are used here and differences in flux climatologies are presented. This comparative study is divided into two parts; one dealing with CERES-SSF data using instantaneous cloud-free measurements and the other using monthly average fluxes from CERES-EBAF. In the following subsection, a brief summary of the literature relevant in this area is discussed.

4.1 Literature Review

Previous works have compared satellite data with radiative transfer model using analyzed data. *Kiehl and Briegleb* [1992] describes such comparison by employing atmospheric profiles of temperature and water vapor from ECMWF analyses and NMC sea surface temperatures. In this article, the radiative transfer model uses analyses data in calculating longwave clear-sky fluxes over ocean surfaces, that are compared to ERBE-retrieved fluxes. Significant differences in calculated fluxes over the ITCZ and subtropical region was observed for the month of July. Particularly, region of largest biases for July, 1989, corresponded to high clouds and deep convection associated with strong upward motion. *Kiehl and Briegleb* [1992] argues that these biases correspond to errors due to cloud contamination and moisture variability related to convection. They show that upper tropospheric moisture is important in clear-sky OLR climatology. However, modeled clear-sky OLR were found to be in agreement with the ERBE retrieved flux over most parts.

A comprehensive study of calculated clear-sky fluxes from reanalyses is given in *Slingo et al.* [1998] that includes flux distribution over both land and ocean surfaces. This study uses ERA project to simulate $\mathrm{OLR}_{clear-sky}$ using an improved clear-sky simulation and humidity analyses. These estimates were compared to ERBE satellite

data on global, zonal and regional scales. ERBE missing data mask for each month was applied to ERA data for consistency. It was found that ERA and ERBE clear-sky fluxes were in good agreement over oceans due to improvement in humidity structure. Although, significant differences were identified in low latitude regions over ITCZ and subtropics. Large biases between ERA and ERBE OLRs were observed over land; the Saharan and the Arabian Desert, the Eurasian landmass, parts of North America and the Antarctica showed differences throughout the year. Many seasonal disagreements were observed in the southern hemisphere land as well. *Slingo et al.* [1998] goes on to identify that errors in surface temperature analyses over certain land regions were responsible for the differences. Differences over the convective regions of the ocean were attributed to systematic errors in ERBE clear-sky diagnostics.

Further comparison was done in *Allan et al.* [2008], using ERA-40 reanalysis and multiple satellite instrument over the period 1979-2002. In adjunct, comparisons with the NCEP/NCAR reanalysis and the Hadley Centre atmospheric climate model, HadAM3 were also made. This study features both longwave and shortwave radiative diagnostics of ERA-40. The article emphasized clear-sky OLR regional difference to errors in humidity analyses in the tropics and temperature differences over higher latitudes. It was also shown that using satellite like sampling in clear-sky OLRs, reduced the discrepancies over moist equatorial zone as a result of dry sampling of reanalysis data.

We now look at the comparisons of MERRA and ERA-Interim fluxes with CERES instrument fluxes. Note that the results mentioned above are specific to the models used and may not apply to our results.

4.2 Results of Comparison

The comparisons were carried out in two parts. The first part comprises instantaneous flux measurement of CERES-SSF data. This is similar to Method 1 definition, which chooses only cloud-free footprints from CERES instruments. The

second part uses CERES-EBAF dataset which provides monthly average clear-sky flux data. Note that CERES data employed here were not included as observational input to the two reanalysis and is, therefore, independent of them.

4.2.1 Reanalysis with SSF

In this subsection, a direct comparison of reanalysis calculations with individual CERES flux measurements is made. MERRA and ERA-Interim are the latest reanalysis product that provide clear-sky flux value at each regional grid, on hourly and three-hourly time steps respective. This configuration provides a complete global coverage at each time step and is used in matching fluxes with instantaneous CERES-SSF measurements.

Cloud-free footprints from SSF are identified if they satisfy three conditions: (i) 'Cloud-mask clear-strong percent coverage' parameter of a FOV must be greater than 96%, (ii) 'Radiance and Mode flags' bits 2-7 must be zero to ensure good quality of measurement and (iii) LW and SW TOA flux must not be of default value. For each cloud-free FOV, a reanalysis flux value is determined by spatially interpolating the nearest-time reanalysis field to the FOV location. Monthly distributions are constructed by organizing all cloud-free FOVs in that month on regional grids and averaging them. In this comparison, a grid dimension of 1^o by 1^o was chosen. The flux difference of the reanalysis and SSF is, therefore, determined by averaging individual flux differences in a grid box.

This kind of distribution is similar to Method 1 definition used in evaluating GCMs with satellite data. Clearly, no diurnal averaging is involved and only cloud-free data were taken into consideration. This construction results in many missing data on the globe, particularly towards the polar regions and areas of persistent cloudiness. Caution must be taken when evaluating global averages for these distributions. Area weighted averages are avoided in presence of missing data and latitudinally weighted zonal averages are used.

Note that the resultant distributions are true for only cloud-free scene. Since, only cloud-free footprints from SSF were included, reanalysis data collocated in space and time will most likely reflect similar clear-sky conditions. Although, discrepancies may arise due to difference in spatial resolution; MERRA and ERA-Interim archive fluxes on larger grid area as compared to CERES footprint area. Similarly, comparing instantaneous measurements with time averaged fluxes may give rise to spurious errors. The following subsections explain the results for OLR and RSW distribution. We choose the SSF product of Flight Model 1 instrument on Terra satellite, for the month of January and July, 2008.

(i) $\mathrm{OLR}_{clear-sky}$

The global average differences between MERRA and SSF $\mathrm{OLR}_{clear-sky}$ were found to be 5.6 W/m^2 for January and 5.0 W/m^2 for July of 2008. These values exceed the uncertainty in CERES OLR measurements taken to be 1.0 W/m^2 for regional average fluxes [*Loeb et al.*, 2007].

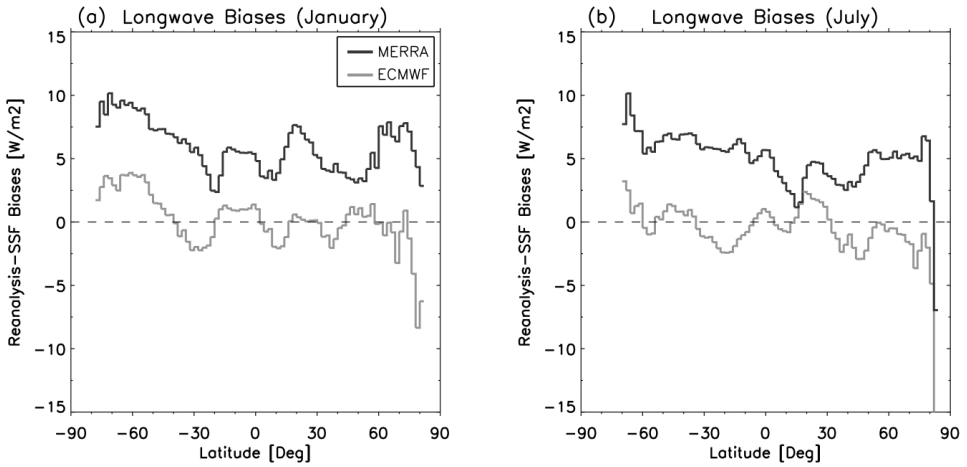

Fig. 4.1. Zonal average of reanalysis minus SSF for $\mathrm{OLR}_{clear-sky}$ for (a) January and (b) July 2008.

This implies that MERRA $\mathrm{OLR}_{clear-sky}$ values are systematically high. In comparison, global biases between ERA-Interim and SSF are 0.1 W/m^2 for January and

-0.4 W/m^2 for July, showing good agreement. Also, the bias magnitude for the reanalyses varies less between the two months.

To explore further, the zonal average OLR$_{clear-sky}$ differences for both reanalysis are plotted in Figure 4.1. Biases in MERRA are found to be of 3-10 W/m^2 magnitude for both months. This indicates that MERRA OLR$_{clear-sky}$ are overestimated compared to SSF measurements over most latitudes. In addition, Figure 4.1 shows that the agreement between SSF and ERA-Interim is consistently good at most latitudes leading to low biases globally.

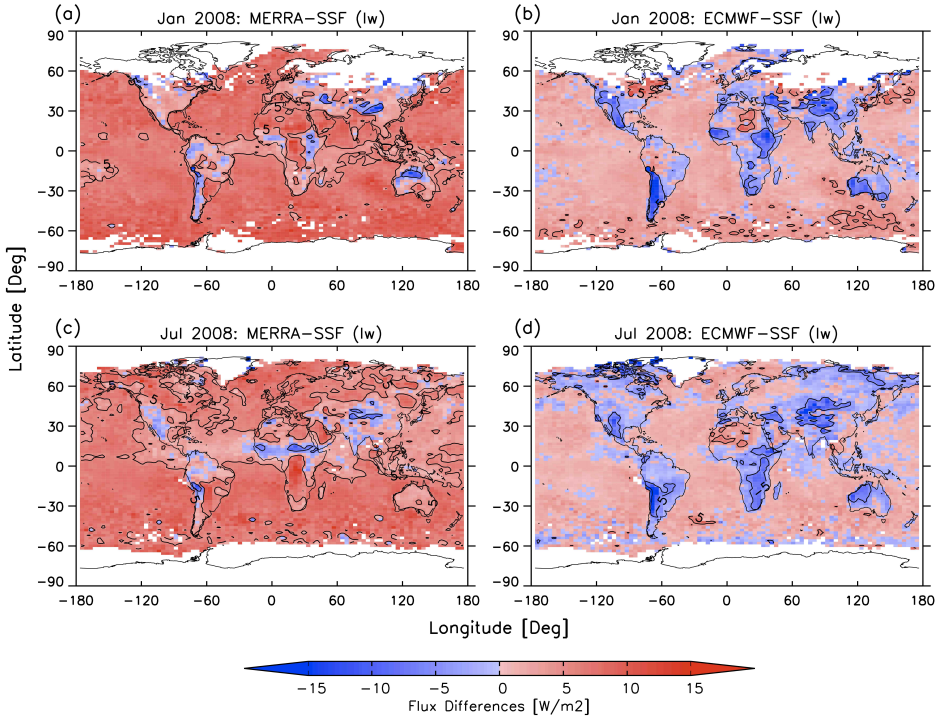

Fig. 4.2. Global distribution of reanalysis minus SSF for OLR$_{clear-sky}$ for (a),(b) January and (c),(d) July of 2008. Contours show values of $\pm$ 5 W/m^2 differences.

Figure 4.2 shows the spatial distribution of $\mathrm{OLR}_{clear-sky}$ differences on a global plot. We use a bi-coloring scheme to each lat-lon grid to display the differences. Contours of $\pm$ 5 W/m^2 are plotted to indicate large differences. With few exceptions, the distribution for January and July appear the same. MERRA and ERA-Interim both overestimate fluxes for most parts of ocean, whereas, interesting features appear over land domain. ERA-Interim shows mostly negative differences over land with western Australia, central Asia, Africa, western North America and South America depicting large biases. Thus, while there is reasonable agreement in the global and zonal averages for ERA-Interim, this agreement hides much larger compensating differences in the spatial field. For MERRA, differences over land are mostly positive with a few regions of negative biases. Overall, the differences in MERRA have a relatively constant magnitude over most parts of the globe. We reckon that high biases (global and zonally) in MERRA arise due to large differences over ocean regions.

(ii) $\mathrm{RSW}_{clear-sky}$

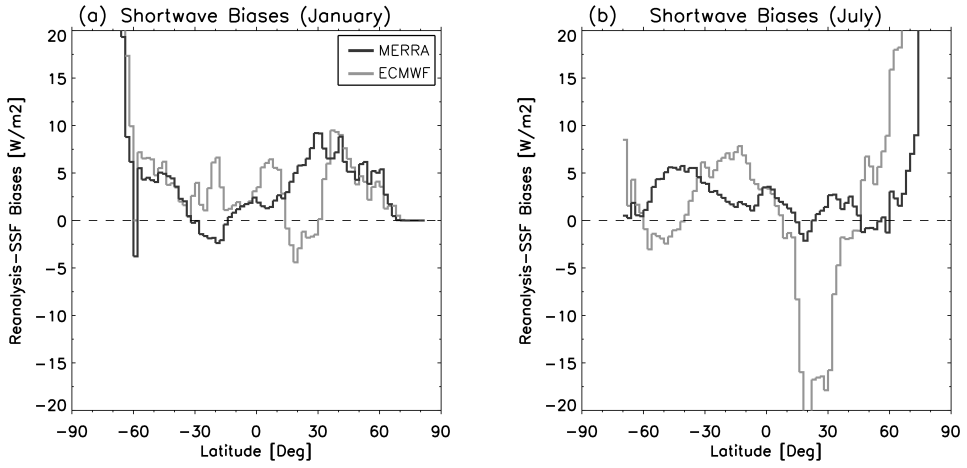

Fig. 4.3. Zonal average of reanalysis minus SSF for $\mathrm{RSW}_{clear-sky}$ for (a) January and (b) July 2008.

The global average differences between MERRA and SSF $RSW_{clear-sky}$ are 4.4 W/m^2 for January and 2.8 W/m^2 for July. These are found to be beyond the uncertainty of RSW CERES measurements, taken as 1.5 W/m^2 for regional average fluxes [*Loeb et al.*, 2007]. The global average biases between ERA-Interim and SSF (5.9 W/m^2 for January and 1.7 W/m^2 for July) also exceed the CERES uncertainty, suggesting that ERA-Interim $RSW_{clear-sky}$ values are systematically high. In contrast to the $OLR_{clear-sky}$ results, $RSW_{clear-sky}$ biases vary significantly for the two months.

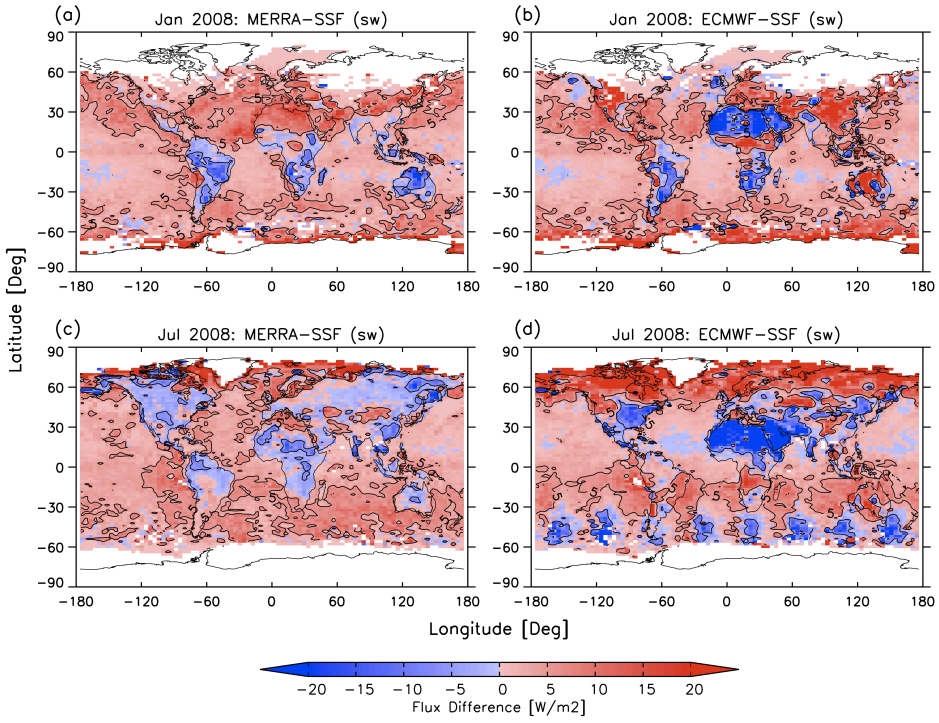

Fig. 4.4. Global distribution of reanalysis minus SSF for $RSW_{clear-sky}$ for (a),(b) January and (c),(d) July of 2008. Contours show values of $\pm$ 5 W/m^2 differences.

Figure 4.3 depicts the zonal average $RSW_{clear-sky}$ differences. MERRA, for most latitudes, overestimates $RSW_{clear-sky}$, whereas errors in ERA-Interim vary in large

magnitude along latitudes. For example, large zonal differences in July at 25^o N are present in ERA-Interim due to regional differences over the Sahara and the Middle East.

Figure 4.4 shows the regional distribution of $\mathrm{RSW}_{clear-sky}$ differences. MERRA biases are positive over the ocean and mostly negative over continents. Exception to this is the northern hemisphere land that exhibit positive differences in January. On the other hand, ERA-Interim shows positive biases over the oceans. The continents are a mixed bag, with the Sahara and parts of the Middle East showing large negative differences in both months, and summertime high-latitudes showing large positive values. Also, apparent in ERA-Interim data are a series of negative maxima located during July at about 50^oS. These are due to the 3-hour archiving of ERA-Interim data, and a similar pattern emerges if we resample MERRA to 3-hourly data (not shown).

4.2.2 Reanalysis with EBAF

The previous subsection describes a direct comparison of cloud-free CERES FOVs against corresponding values of clear-sky fluxes from the reanalyses. Discrepancies in those comparisons can roughly be attributed to errors in either CERES measurements or reanalysis calculations. In this subsection, we compare monthly mean clear-sky fluxes of reanalysis with monthly mean values from CERES-EBAF dataset. As mentioned earlier, EBAF clear-sky fluxes are derived from CERES and MODIS clear-sky radiances. This approach is useful in improving the flux quality making it suitable for evaluation purposes.

Regional EBAF data are available on 1^o by 1^o grid resolution in monthly averaged quantities. For this comparison, we spatially interpolate and arrange the reanalysis data to EBAF resolution and subtract flux values grid by grid. Since, EBAF has a complete global coverage of clear-sky fluxes, area weighted mean of fluxes was used to estimate global averages.

Table 4.1
Global monthly mean clear-sky fluxes (March 2000 - October 2005) from CERES-EBAF, MERRA and ERA-Interim.

		January	April	July	October	Annual
OLR (W/m^2)	EBAF	265.9	268.9	274.1	268.9	269.5
	MERRA	265.1	267.3	271.8	268.5	268.2
	ERA-Interim	261.1	263.5	267.7	264.1	264.1
RSW (W/m^2)	EBAF	54.1	54.1	48.7	52.3	52.3
	MERRA	54.2	53.0	49.8	52.0	52.3
	ERA-Interim	55.5	53.8	50.4	54.4	53.6

Table 4.1 lists the global means for $\mathrm{OLR}_{clear-sky}$ and $\mathrm{RSW}_{clear-sky}$ fluxes over the period of March 2000 to October 2005. The agreement between EBAF and MERRA is within 1-2 W/m^2 for both $\mathrm{OLR}_{clear-sky}$ and $\mathrm{RSW}_{clear-sky}$. ERA-Interim $\mathrm{OLR}_{clear-sky}$ are $\sim$ 5 W/m^2 lower than the EBAF, while $\mathrm{RSW}_{clear-sky}$ values are within 1-2 W/m^2. The amplitude of annual cycle in EBAF (8.2 W/m^2 for $\mathrm{OLR}_{clear-sky}$ and 5.4 W/m^2 for $\mathrm{RSW}_{clear-sky}$) exceeds that in MERRA (6.7 W/m^2 for $\mathrm{OLR}_{clear-sky}$ and 4.4 W/m^2 for $\mathrm{RSW}_{clear-sky}$) and ERA-Interim (6.6 W/m^2 for $\mathrm{OLR}_{clear-sky}$ and 5.1 W/m^2 for $\mathrm{RSW}_{clear-sky}$). The following describes the result for $\mathrm{OLR}_{clear-sky}$ and $\mathrm{RSW}_{clear-sky}$ comparisons with EBAF:

(i) $\mathrm{OLR}_{clear-sky}$

Figure 4.5 shows the zonal distribution of $\mathrm{OLR}_{clear-sky}$ differences between the reanalyses and EBAF. Note that these biases are averaged over the time period, March 2000 to October 2005. ERA-Interim and MERRA zonal differences show almost similar latitudinal variations, although EBAF $\mathrm{OLR}_{clear-sky}$ agree better with MERRA than with ERA-Interim. For example, in July, ERA-Interim biases are shown to be negative over most latitude. This can be contrasted to the comparison

of cloud-free FOVs in Figure 4.1, that showed better agreement with ERA-Interim clear-sky fluxes.

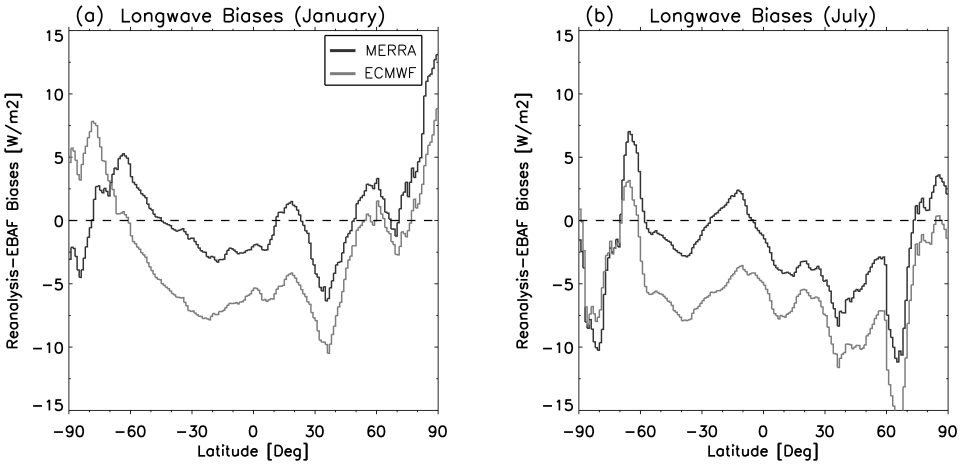

Fig. 4.5. Zonal average of monthly reanalysis minus EBAF for $\mathrm{OLR}_{clear-sky}$ for (a) January and (b) July averaged over March 2000 - October 2005.

Figure 4.6 depicts the spatial distribution of the differences. Over the oceans, Figure 4.6 shows patterns of positive and negative values. The positive values tend to occur in regions of persistent low-level clouds, such as off the west coast of North and South America. Sea coast of Antarctica is also highlighted by positive biases for both months. This is quite different from the comparison in Figure 4.2, where most parts of the oceans showed positive values. Over land, the ERA-Interim biases are mostly negative, especially in July. Whereas, in MERRA, a mix of positive and negative regional biases are observed. There is, overall, a high degree of similarity between the MERRA and ERA-Interim comparisons.

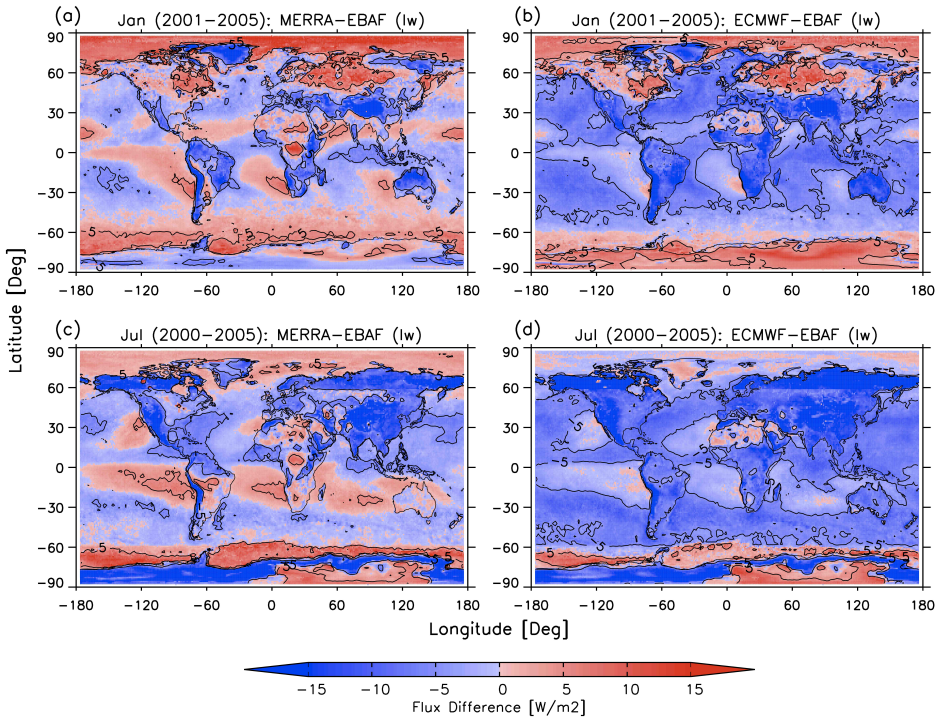

Fig. 4.6. Global distribution of monthly reanalysis minus EBAF for $OLR_{clear-sky}$ for (a),(b) January and (c),(d) July averaged over March 2000 - October 2005. Contours show values of ± 5 W/m^2.

(ii) $RSW_{clear-sky}$

The global mean differences in $RSW_{clear-sky}$ for MERRA are 0.1 W/m^2 in January and 1.1 W/m^2 in July. In comparison, this is smaller than ERA-Interim values of 1.4 W/m^2 in January and 1.6 W/m^2 in July. Figure 4.7 shows the zonal distribution of $RSW_{clear-sky}$ differences between the reanalyses and EBAF. Agreement with EBAF is within ± 5 W/m^2, except near the summer pole. This shows that regions of high $RSW_{clear-sky}$ correspond to large biases.

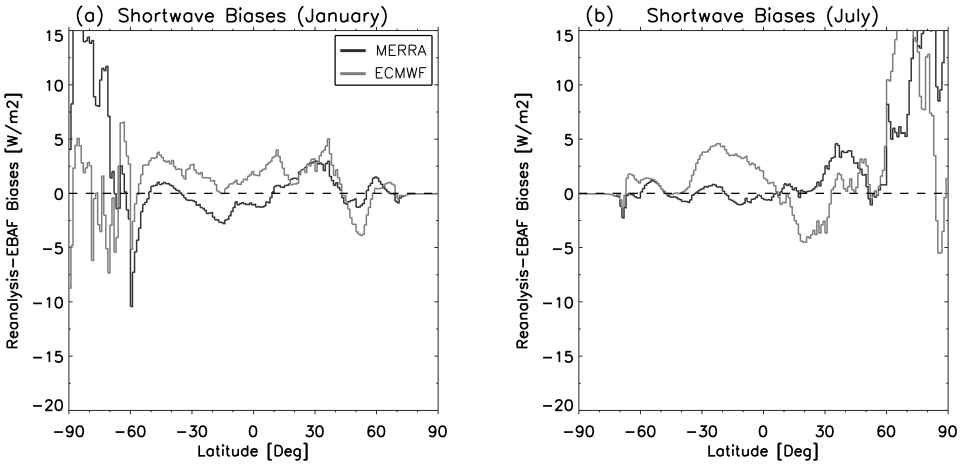

Fig. 4.7. Zonal average of monthly reanalysis minus EBAF for $\mathrm{RSW}_{clear-sky}$ for (a) January and (b) July averaged over March 2000 - October 2005.

Figure 4.8 shows the spatial distribution of the differences in $\mathrm{RSW}_{clear-sky}$. In MERRA data, the largest differences are located at high summer latitudes. This include high biased polar regions where $\mathrm{RSW}_{clear-sky}$ concentrations are large. In ERA-Interim, the largest differences are present over land. Discrete land surface properties lead to biases of varying signs. For example, the Saharan Desert in Africa is shown to be negatively biases where as the Tibetan Plateau appears with positive biases. Smaller differences occur over the oceans, and these are also of positive and negative signs. This is in contrast to the previous comparison in Figure 4.4 where only positive biases are present over the oceans. Unlike the $\mathrm{OLR}_{clear-sky}$ comparison in Figure 4.6, there is no clear correspondence between the ocean differences and the distribution of clouds.

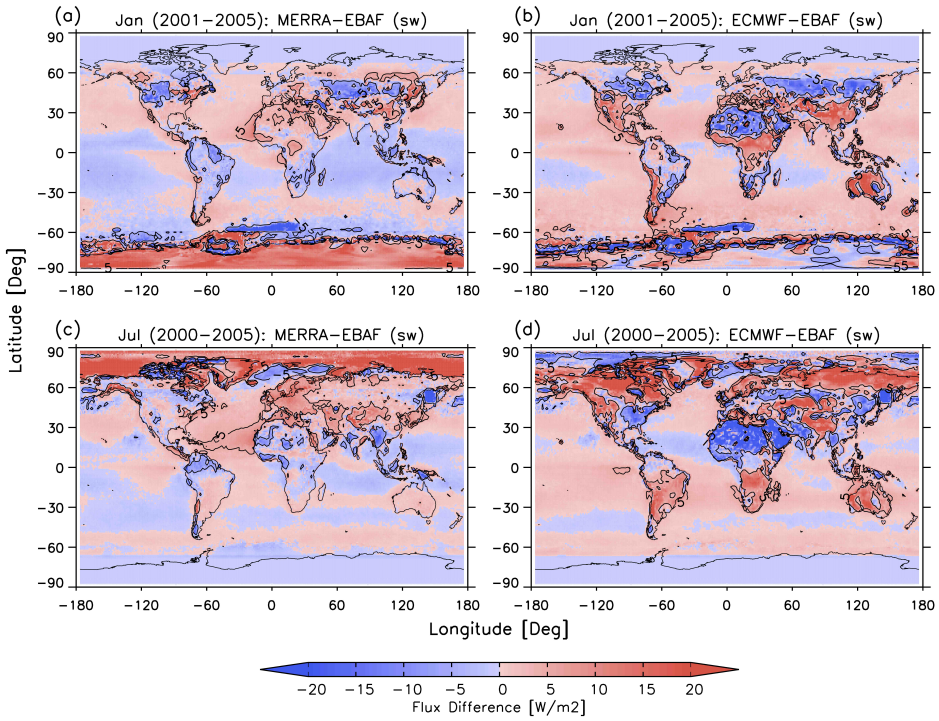

Fig. 4.8. Global distribution of monthly reanalysis minus EBAF for $\mathrm{RSW}_{clear-sky}$ for (a),(b) January and (c),(d) July averaged over March 2000 - October 2005. Contours show values of $\pm$ 5 W/m^2.

4.3 Summary

We present our analysis of clear-sky fluxes of MERRA and ERA-Interim reanalysis with satellite-inferred fluxes. Comparisons with cloud-free CERES footprints from SSF is given in subsection 4.2.1. Distribution of $\mathrm{OLR}_{clear-sky}$ in Figure 4.2 shows that MERRA overestimates flux values over most part of the globe leading to large global biases. Figure 4.4 depicts $\mathrm{RSW}_{clear-sky}$ regional distribution where large discrepancies exist in most parts of the globe.

This is followed by subsection 4.2.2, that explains the comparisons with monthly averaged EBAF. Table 4.1 lists the global averages over different seasonal cycles. The

$OLR_{clear-sky}$ differences are described from Figure 4.6 where similarities in MERRA and ERA-Interim biases are drawn. Regional plots in Figure 4.8 show $RSW_{clear-sky}$ values that highlight discrepancies over regions of high flux concentration. Overall, a quantitative assessment of clear-sky fluxes from the reanalyses is provided in this section.

5. VARIABILITY IN CLEAR-SKY FLUXES

In the study of climate change, the focus is mainly on the departures from average seasonal cycle, also known as inter-annual anomalies. This section deals with our analysis of inter-annual variability expressed in clear-sky TOA fluxes. A comparative study of clear-sky flux anomalies using satellite and model-derived data is explained here.

5.1 Issues in Clear-sky Fluxes

Before describing the variability in clear-sky fluxes, its important to mention certain issues concerning clear-sky data. Clear-sky TOA flux, usually, is derived from radiative transfer simulation or cloud-free satellite observations. These are separate estimates of fluxes and, for most cases, are inconsistent with one another. The sources of discrepancy in satellite and model-derived fluxes can be summed up as (i) difference in cloudiness representations, (ii) difference in atmospheric structure, for example, tropospheric temperature and humidity distribution and (iii) inconsistency in the spatial location of dynamical regimes (convection and subsidence regions). Many literatures have shown the existence of such disagreements as a result of sampling issues.

Work done by [*Allan and M.A.Ringer*, 2003] suggest that monthly clear-sky OLR measurements are inconsistent with mean vertical motion fields in climate model. This is to imply that satellite sampling mostly corresponds to weaker ascent regions, thereby, biasing global averages in CRFs. *Sohn et al.* [2006] shows that satellite-estimated longwave CRFs also include radiation perturbation due to water vapor changes related to cloud formation. Due to the fact, that satellites are unable to measure clear-sky fluxes over overcast regions, the upper tropospheric humidity distributions tend to be drier than mean condition causing large magnitude of biases. Furthermore, satellite sampling causes discrepancies in total columnar water va-

por distribution of the boundary layers as described in *Sohn and Bennartz* [2008]. Therefore, its important that spatial resolution of satellite instruments be improved, to allow detection of cloud-free pixels near cloud edges or between broken cloud fields. Such pixels are considerably moist in upper troposphere and would result in an overall reduction in dry bias. CERES-EBAF dataset uses MODIS pixels (of 2km resolution) from cloudy footprint to infer cloud-free fluxes, thereby improving the overall quality of flux data.

Issues in deriving shortwave CRF arises due to inaccurate mapping of aerosol content in the models. Climate models often employ climatological background of aerosol profiles, that do not match with satellite samplings. Because of the complex interaction between cloud hydrometeors and aerosol particles, there is ambiguity in choosing model-derived $\mathrm{RSW}_{clear-sky}$ for CRF calculations. *Erlick and Ramaswamy* [2003] highlights this case by analyzing clear-sky conditions with and without the presence of aerosol content, where large differences in regional RSW fluxes were observed.

Hence, handling clear-sky flux data requires a thorough knowledge of these issues involved.

5.2 Comparison of Monthly Average EBAF $\mathrm{R}_{clear-sky}$ Anomalies

In this subsection, we compare anomalies in EBAF $\mathrm{OLR}_{clear-sky}$, $\mathrm{RSW}_{clear-sky}$ and $\mathrm{R}_{clear-sky}$ with anomalies in MERRA and ERA-Interim. Inter-annual anomaly of clear-sky fluxes is calculated over the entire time series (in this case, March 2000 to October 2005). This can be mathematically expressed as:

$$F_{anom} = F_{mon} - \overline{F_{mon}}$$

where F_{anom} is the flux anomaly of a given month, F_{mon} and $\overline{F_{mon}}$ are current and average fluxes for the month. For example, to calculate flux anomaly for January

2003, we average fluxes from all months of January and subtract it from the flux value of January 2003. For interannual anomalies, its important that seasonality trend among the fluxes be removed. For this reason, we take the mean flux values of a particular month. Such anomaly is commonly referred as 'deseasonalized'. The quantity, F_{anom} is calculated each month for EBAF, MERRA and ERA-Interim fluxes separately. Regional F_{anom} are derived by calculating anomalies on each lat-lon grid.

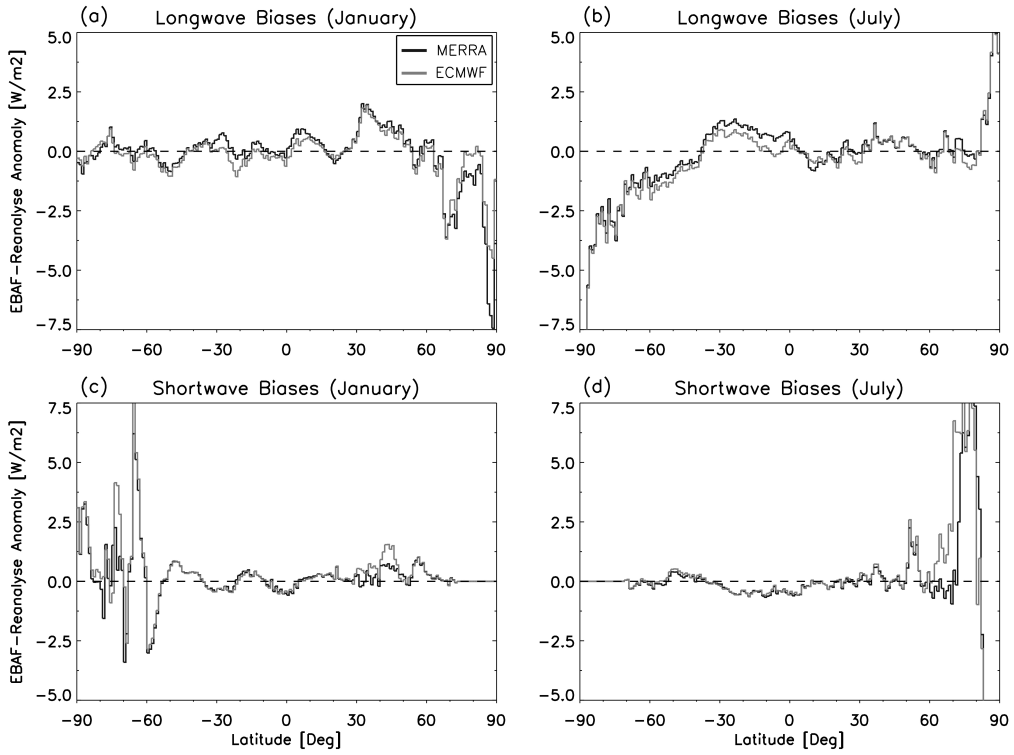

Fig. 5.1. Zonal average of EBAF anomalies minus reanalysis anomalies for (a) and (b) $OLR_{clear-sky}$ and (c) and (d) $RSW_{clear-sky}$ for January and July of 2001.

Figure 5.1 shows the zonal average differences in anomalies between EBAF and the reanalyses for January and July, 2001. The agreement between the two is good for all zones, except in high winter latitudes for $OLR_{clear-sky}$ anomalies and in high summer latitudes for $RSW_{clear-sky}$ anomalies.

Fig. 5.2. $\mathrm{OLR}_{clear-sky}$ anomalies distribution for CERES-EBAF and MERRA for January, March, May, July, September, and November of 2001. The third column is a scatter plot of individual grid points, with each point representing flux averaged over a fixed area. A linear fit is also shown, which depicts the first EOF of the dataset.

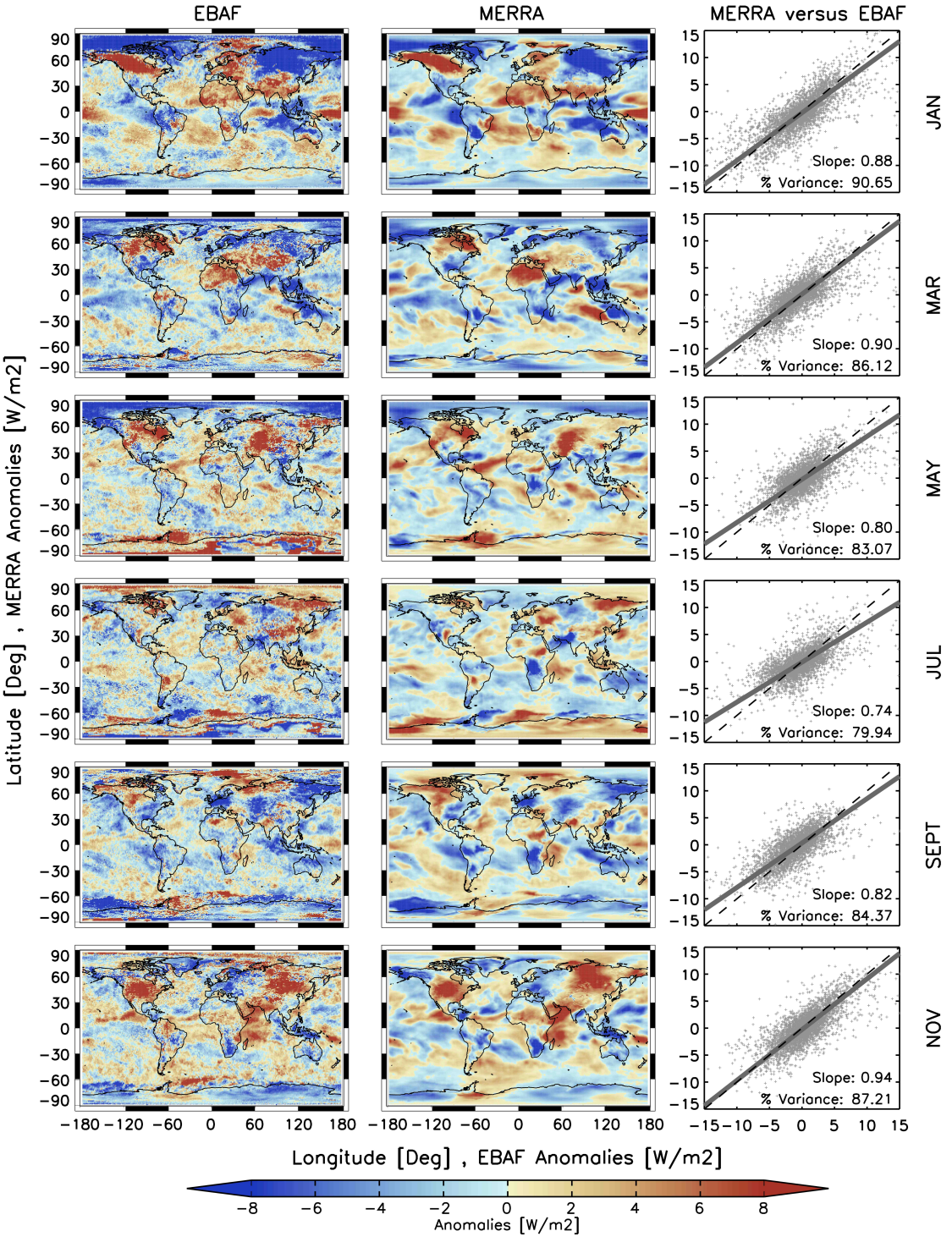
EBAF
MERRA
MERRA versus EBAF
JAN
MAR
MAY
JUL
SEPT
NOV
Slope: 0.88
% Variance: 90.65
Slope: 0.90
% Variance: 86.12
Slope: 0.80
% Variance: 83.07
Slope: 0.74
% Variance: 79.94
Slope: 0.82
% Variance: 84.37
Slope: 0.94
% Variance: 87.21
Latitude [Deg] , MERRA Anomalies [W/m2]
Longitude [Deg] , EBAF Anomalies [W/m2]
Anomalies [W/m2]

Fig. 5.3. $\mathrm{RSW}_{clear-sky}$ anomalies distribution for CERES-EBAF and MERRA for January, March, May, July, September, and November of 2001. The third column is a scatter plot of individual grid points, with each point representing flux averaged over a fixed area. A linear fit is also shown, which depicts the first EOF of the dataset.

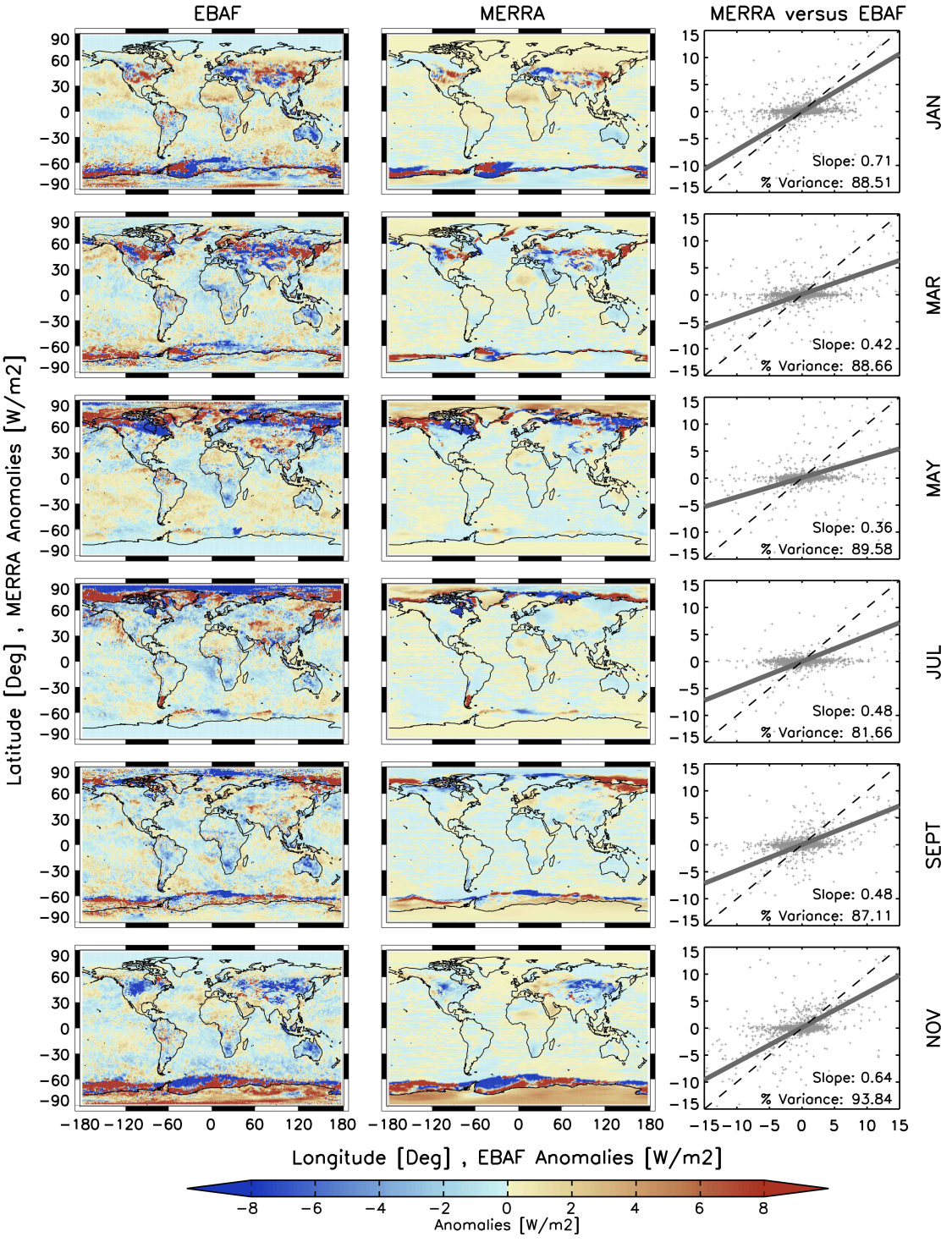
EBAF
MERRA
MERRA versus EBAF
JAN
MAR
MAY
JUL
SEPT
NOV
Slope: 0.71
% Variance: 88.51
Slope: 0.42
% Variance: 88.66
Slope: 0.36
% Variance: 89.58
Slope: 0.48
% Variance: 81.66
Slope: 0.48
% Variance: 87.11
Slope: 0.64
% Variance: 93.84
Latitude [Deg] , MERRA Anomalies [W/m2]
Longitude [Deg] , EBAF Anomalies [W/m2]
Anomalies [W/m2]

The clear implication is that, while there are differences of several W/m^2 in flux magnitudes, as shown in the previous section, these biases are removed in the anomalies. This was previously seen in other clear-sky diagnostics by *Allan and M.A.Ringer* [2003] which uses ERA-40 reanalysis. Also note, that the differences for the two reanalysis, matches with each other. The agreement between the two reanalysis is excellent as they agree to within few tenths of a W/m^2 at most latitudes (not shown here). In the following figures, we show the results for MERRA reanalysis only.

Figure 5.2 shows the spatial distribution of OLR$_{clear-sky}$ anomalies for EBAF and MERRA for the months of January, March, May, July, September, and November of 2001. Anomalies from ERA-Interim are in close agreement with MERRA and hence are not shown. The first two columns shows the regional OLR$_{clear-sky}$ anomalies in EBAF and MERRA, respectively. Same coloring scheme is applied to the two regional distributions. The third column in the figure is a scatter plot of individual grid points, with each point representing the flux anomaly averaged over a fixed area. The x and y axis are denoted by EBAF and MERRA anomalies, respectively. A linear fit is also shown, which we calculate as the first EOF of the dataset. As shown, regional patterns of anomalies found in MERRA are similar to those in EBAF. There is close agreement at the grid-point level, with slopes nearing one and high explained variance in each month.

Figure 5.3 shows the same comparison for RSW$_{clear-sky}$. Overall, the anomaly pattern in the observations and the reanalysis correspond closely. The anomalies are larger and more comparable in the polar regions. Likewise, large anomaly patterns are visible over land and near polar regions in each month. However, there are quantitative differences, with MERRA showing anomalies that are a factor of 5-10 smaller than EBAF over most of the globe. The combination of these leads to a slope of the global correlation to average around 0.5.

Figure 5.4 shows the time series of monthly global average anomalies for the period of March 2000 to October 2005. The RMS difference between EBAF and MERRA (ERA-Interim) time series is 0.26 (0.30) W/m^2 for OLR$_{clear-sky}$, 0.23 (0.27) W/m^2 for RSW$_{clear-sky}$, and 0.33 (0.36) W/m^2 for R$_{clear-sky}$. Overall, it is clear that the observations and reanalyses are highly correlated, with MERRA showing stronger correlations with the observations (correlation coefficient r = 0.79, 0.69, 0.65 for OLR$_{clear-sky}$, RSW$_{clear-sky}$, R$_{clear-sky}$, respectively) than ERA-Interim (r = 0.70, 0.40, 0.54). It is also obvious that the observations, particularly the RSW$_{clear-sky}$, show higher month-to-month variations than the reanalyses do.

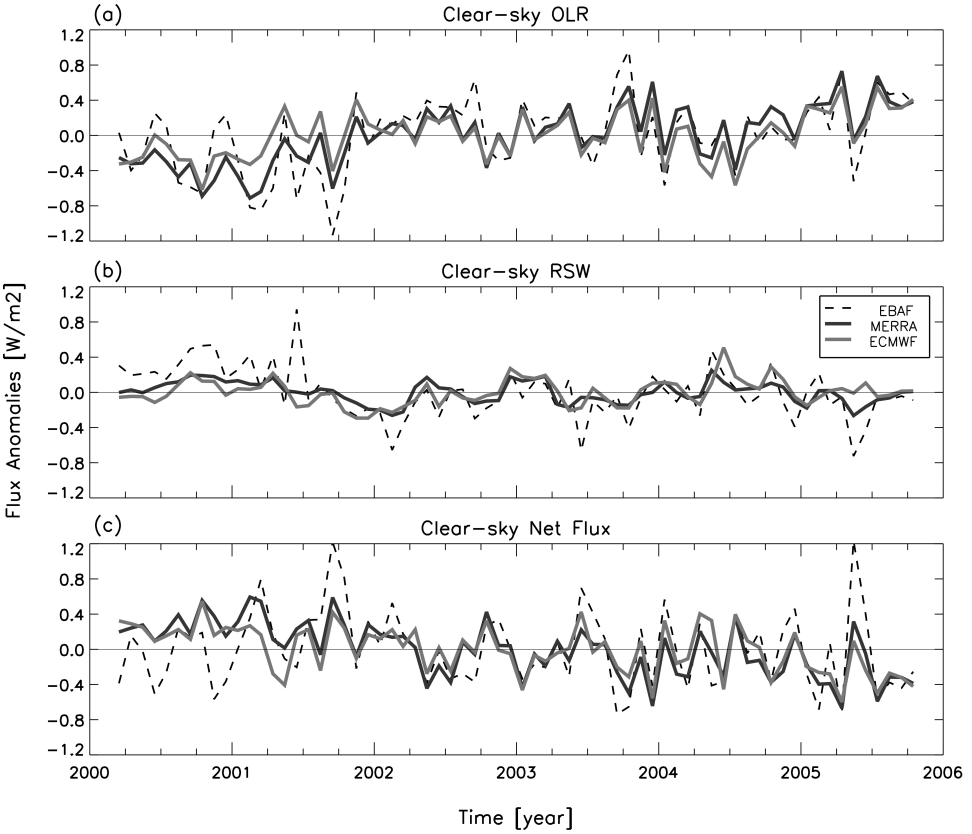

Fig. 5.4. Time series of global monthly average anomalies of TOA clear-sky (a) OLR, (b) RSW and (c) Net Incoming flux from CERES-EBAF, MERRA and ERA Interim (March 2000 to October 2005).

An important reference in comparing inter-annual variability in clear-sky fluxes is given in *Allan et al.* [2008]. Analysis of inter-annual anomalies in $\mathrm{OLR}_{clear-sky}$ were performed using ERA-40, NCEP, ScaRaB and CERES data from low latitude regions. Variations in column water vapor correlated with the clear-sky OLR anomalies, although the simulated fluxes were not in agreement. Overall, the comparison showed much poorer agreement than we see here. This is not surprising since both the observations and the reanalysis have significantly improved over the last decade.

6. SUMMARY

Cloud-radiative interactions involve complex mechanisms which create large uncertainty in climate change projections. They are often expressed in terms of cloud radiative forcings which are evaluated using clear-sky fluxes [*Dessler*, 2010]. The concept of clear-sky fluxes is based on the hypothetical condition of non participation of cloud hydrometeors in the radiational budget. This quantity is inferred by two methods; one is to use cloud-free measurements from satellite instruments [*Ramanathan et al.*, 1989] and the other is to use clear-sky radiative transfer calculations.

Depending on the method, various issues arise in the usage of clear-sky fluxes, as there exist considerable disagreements among the two definitions. *Cess and Potter* [1986] points out that model-derived fluxes be sampled to resemble satellite-inferred fluxes. Limitations in model schemes exist in simulating hydrological cycle, atmospheric circulation, cloud properties, aerosol distribution etc. Moreover, satellite-inferred clear-sky fluxes suffer from inherent dry biases [*Sohn and Bennartz*, 2008; *Sohn et al.*, 2006] and calibration errors in measurements [*Loeb et al.*, 2009].

In recent years, improvements have been made to circumvent these issues. CERES-EBAF, a new product from the CERES team, incorporates clear-sky fluxes from small spatial scales, proved to decrease dry biases. Latest reanalysis product from MERRA and ERA-Interim, now have improved hydrological representation, better data assimilating system and reliable forecast model. We use these products in our analysis of TOA clear-sky fluxes and compare them in terms of biases and inter-annual anomalies.

We approach our comparative study in two ways. Our first analysis uses cloud-free measurements archived from CERES-SSF product and compares them with the reanalyses. There is no sampling bias in this comparison since data from reanalysis resemble clear-sky conditions. Global $\mathrm{OLR}_{clear-sky}$ biases in MERRA are found to be systematically high, whereas, ERA-Interim show better agreement with SSF.

Although, regional distribution in Figure 4.2 showed large compensating difference over land for ERA-Interim. $RSW_{clear-sky}$ biases in Figure 4.4, on the other hand, were depicted in regional patterns over most parts of the globe. Our second comparison uses monthly average CERES-EBAF data against monthly averaged reanalysis fluxes. The patterns of agreement and disagreement for this comparison, shown in Figure 4.6 and 4.8, are different than for the comparisons involving CERES-SSF, suggesting that sampling may be an issue. The magnitude of disagreement for both comparisons are found to be less than 5-10 W/m^2.

Our final comparison was for inter-annual anomalies, that are calculated by subtracting the mean annual cycle. Despite biases between EBAF and the reanalysis fluxes of several W/m^2, the agreement between observed anomalies and those from the reanalysis were quite good, with zonal mean differences generally less than 1 W/m^2 in Figure 5.1. Thus, the subtraction of the mean annual cycle also subtracted off majority of bias. Analyses of spatial distribution of the anomalies in Figure 5.2 and 5.3 found that patterns in the observations agreed well with those in the reanalyses. $OLR_{clear-sky}$ anomalies in the observations were close in magnitude to those in the reanalyses. For $RSW_{clear-sky}$, however, the reanalysis anomalies over most parts of the globe were a factor of 5-10 smaller than the observed anomalies.

Finally, we compared the time series of the anomalies shown in Figure 5.4. They are highly correlated and show similar variations in time, with the anomalies in the observations showing larger month-to-month variations. Ultimately, it is not possible to determine which dataset should be considered more correct; there are advantages and disadvantages to both the measurements and the reanalyses. For many applications, however, it should be possible to use either of these products.

REFERENCES

Allan, R., and M.A.Ringer (2003), Inconsistencies between satellite estimates of longwave cloud forcing and dynamical fields from reanalyses, *Geophysical Research Letters*, *30*, 44.

Allan, R., M. Ringer, J. Pamment, and A. Slingo (2008), Simulation of the earth radiation budget by the european center for medium-range weather forecasts 40-year reanalysis (era40), *Journal of Geophysical Research*, *113*, D20,107.

Cess, R., and G. Potter (1986), Exploratory studies of cloud radiative forcings with a general circulation model, *Tellus(1987)*, *39A*, 460–473.

Cess, R., G. Potter, W. Gates, J.-J. Morcrette, and L. Corsetti (1992), Comparison of general circulation models to earth radiation budget experiment data: Computation of clear-sky fluxes, *Journal of Geophysical Research*, *97*, 20,421–20,426.

Dee, D., S. Uppala, A. Simmons, P. Berrisford, P. Poli, S. Kobayashi, U. Andrae, M. Balmaseda, G. Balsamo, P. Bauer, P. Bechtold, A. Beljaars, L. van de Berg, J. Bidlot, N. Bormann, C. Delsol, R. Dragani, M. Fuentes, A. Geer, L. Haimberger, S. Healy, H. Hersbach, E. Holm, L. Isaksen, P. Kallberg, M. Kohler, M. Matricardi, A. McNally, B. Monge-Sanz, J. Morcrette, B. Park, C. Peubey, P. de Rosnay, C. Tavolato, J. Thepaut, and F. Vitart (2011), The era-interim reanalysis: configuration and performance of the data assimilation system, *Quaterly Journal of the Royal Meteorological Society*, *137*, 553–597.

Dessler, A. (2010), A determination of the cloud feedback from climate variations over the past decade, *Science*, *330*, 1523–1527.

Dessler, A., P.Yang, J.Lee, J. Solbrig, Z. Zhang, and K. Minschwaner (2008), An analysis of the dependence of clear-sky top-of-atmosphere outgoing longwave radiation on atmospheric temperature and water vapor, *Journal of Geophysical Research*, *113*, D17,102.

Erlick, C., and V. Ramaswamy (2003), Note on the definition of clear sky in calculations of shortwave cloud forcing, *Journal of Geophysical Research*, *108(D5)*, 4156.

Hansen, J., L. Nazarenko, R. Ruedy, M. Sato, J. Willis, A. DelGenio, D. Koch, A. Lacis, K. Lo, S. Menon, T. Novakov, J. Perlwitz, G. Russell, G. Schmidt, and N.Tausnev (2005), Earth's energy imbalance: Confirmation and implications, *Science*, *308*, 1431–1435.

Kiehl, J., and B. Briegleb (1992), Comparison of the observed and calculated clear sky greenhouse effect: Implication for climate studies, *Journal of Geophysical Research*, *97*, 10,037–10,049.

Loeb, N., S. Kato, K. Loukachine, and N. Manalo-Smith (2005), Angular distribution models for top-of-atmosphere radiative flux estimation from the clouds and the earth's radiant energy system instrument on the terra satellite. part i: Methodology, *Journal of Atmospheric and Oceanic Technology*, *22*, 338–351.

Loeb, N., B. Wielicki, W. Su, K. Loukachine, W. Sun, T. Wong, K. Priestley, G. Matthews, W. Miller, and R. Davies (2007), Multi-instrument comparison of top-of-atmosphere reflected solar radiation, *Journal of Climate*, *20*, 575–591.

Loeb, N., B. Wielicki, D. Doelling, G. Smith, D. Keyes, S. Kato, N. Manalo-Smith, and T. Wong (2009), Toward optical closure of the earth's top-of-atmosphere radiation budget, *Journal of Climate*, *22*, 748–766.

Ramanathan, V., R. Cess, E. Harrison, P. Minnis, B. Barkstrom, E. Ahmad, and D. Hartmann (1989), Cloud-radiative forcing and climate: Results from the earth radiation budget experiment, *Science*, *243*, 57–63.

Rienecker, M., M. Suarez, R. Todling, J. Bacmeister, L. Takacs, H. Liu, W. Gu, M. Sienkiewicz, R. Koster, R. Gelaro, I. Stajner, and J. Nielsen (2008), The geos-5 data assimilation system - documentation of version 5.0.1, 5.1.0 and 5.2.0, *Release 2 version 1*, NASA Goddard Space Flight Center, Greenbelt, Maryland 20771, Greenbelt, Maryland 20771.

Slingo, A., J. Pamment, and M. Webb (1998), A 15-year simulation of the clear-sky greenhouse effect using the ecmwf reanalyses: Fluxes and comparison with erbe, *Journal of Climate*, *11*, 690–708.

Smith, G., K. Priestley, N. Loeb, B. Wielicki, T. Charlock, P. Minnis, D. Doelling, and D. Rutan (2011), Clouds and earth radiant energy system (ceres), a review: Past, present and future, *Advances in Space Research*, *48*, 254–263.

Soden, B., and I. Held (2006), An assessment of climate feedbacks in coupled ocean-atmosphere models, *Journal of Climate*, *19*, 3354–3360.

Sohn, B., and R. Bennartz (2008), Contribution of water vapor to observational estimated of longwave cloud radiative forcing, *Journal of Geophysical Research*, *113*, D20,107.

Sohn, B., J. Schmetz, R. Stuhlmann, and J. Lee (2006), Dry bias in satellite derived clear-sky water vapor and its contribution to longwave cloud radiative forcing, *Journal of Climate*, *19*, 5570–5580.

Wielicki, B., B. Barkstrom, E. Harrison, R. L. III, G. Smith, and J. Cooper (1996), Clouds and the earth's radiant energy system (ceres): An earth observing system experiment, *Bulletin of the American Meteorological Association*, *77*, 853–868.

Zhang, M., R. Cess, T. Kwon, and M. Chen (1994), Approaches of comparison for clear-sky radiative fluxes from general circulation models with earth radiation budget experiment data, *Journal of Geophysical Research*, *99*, 5515–5523.

VITA

Abhishek Verma received his Bachelor of Technology and Master of Technology degrees in aerospace engineering from the Indian Institute of Technology Madras in 2009. He entered the Master's program of the Department of Atmospheric Sciences at Texas A&M University, College Station in September 2009 and received his Master of Science degree in December 2011. His research interests include climatic variability and satellite remote sensing. He is also interested in studying reanalysis performances and hydrological cycle simulations. He plans to publish a journal article, comparing clear-sky fluxes from satellite observations and reanalysis model.

Mr. Verma may be reached at 1204 Eller O&M Building, Texas A&M University, College Station, Texas 77843-3150, United States. His email address is verma.iitm@gmail.com.